Extreme Emission Line Galaxies Observed with the James Webb Space Telescope's Medium-Band Filters

Sunna Withers

A Thesis Submitted To
The Faculty of Graduate Studies
In Partial Fulfilment of the Requirements
For The Degree Of
Master of Science

Graduate Program in Physics & Astronomy
York University
Toronto, Ontario

October 2023

Abstract

Since the beginning of JWST's science operations, there have been many observations dedicated to finding and characterizing galaxies during the Epoch of Reionization (EoR). This is an important point in the history of the Universe, being the time where the first galaxies began to form and evolve, as well as reionize the neutral Hydrogen that surrounded them. When studying reionization era galaxies, it is of particular importance to identify of faint star-forming galaxies, since these are the galaxies that are thought to be primarily responsible for Hydrogen reionization. Included in the population of star-forming galaxies are Extreme Emission Line Galaxies (EELGs). These are characterized by powerful UV-optical nebular emission lines, driven by elevated levels of star formation. EELGs are abundant in the EoR and have been shown to have properties that suggest they are responsible for reionization, making them ideal targets when searching for galaxies in the EoR.

While many different methods have been used to search for EELGs, medium-band colour selections provide a simple and effective way at searching for them. Extreme emission lines drive extreme colours in medium-band filters which allows EELGs to be selected using medium-band colour cuts. Additionally, medium-band imaging is free of many of the observational challenges associated with more typical selection criteria. To this end, this thesis uses JWST/NIRCam medium-band photometry to search for EELGs. The data used in this work is from the CAnadian NIRISS Unbiased Cluster Survey (CANUCS), which provides deep NIRCam imaging in five broad (F090W, F115W, F150W, F277W, F444W) and nine medium (F140M, F162M, F182M, F210M, F250M, F300M, F335M, F360M, F410M) bands. The depth and extensive use of medium-band filters in CANUCS makes it the ideal data set to search for EELGs at a wide range of redshifts.

We use synthetic CANUCS observations of EELGs to create a colour selection criteria that is used to identify 118 EELGs over $1.7 \lesssim z \lesssim 6.7$, which have both extreme [OIII] + Hβ and Hα emission. We use the medium-band photometry to measure the equivalent widths (EWs) of the galaxies in our sample, finding median $EW(\mathrm{H}\alpha) = 893$ Å and $EW(\mathrm{[OIII]} + \mathrm{H}\beta) = 1255$ Å, as well as some very extreme objects with $EW(\mathrm{[OIII]} + \mathrm{H}\beta) \sim 3000$ Å. Measuring the physical properties of galaxies in our sample reveals that they have properties typical of EELGs: they are mostly compact with low stellar mass (median $\log(M_\star/M_\odot) = 8.03$), low metallicity (median $Z = 0.14Z_\odot$), little dust (median $A_V = 0.18$ mag) and high specific star formation rates (SSFR, median $SSFR = 1.18 \times 10^{-8}/yr$). Finally, we present NIRSpec spectroscopy of 15 of the EELGs in our sample. These spectra confirm the redshifts and EWs of the EELGs calculated from the medium-bands, which demonstrates the accuracy and efficiency of our colour selections. Overall, we show that there are significant advantages to using medium-band photometry to identify and study EELGs across a wide range of redshifts, including galaxies during the EoR.

Contents

List of Tables

List of Figures

1 Introduction

1.1 Extreme Emission Line Galaxies

Extreme emission line galaxies (EELGs) have become a major field of study in recent years, with many searches targeting EELGs in the local Universe up to high-redshifts (e.g. local Universe: Cardamone et al. 2009, Henry et al. 2018, Liu et al. 2022; intermediate-redshift, $z \lesssim 5$: van der Wel et al. 2011, Maseda et al. 2014, Maseda et al. 2018, Tang et al. 2019, Onodera et al. 2020, Tran et al. 2020, Boyett et al. 2022, Gupta et al. 2023; high-redshift, $z \gtrsim 5$: Stark et al. 2013, Smit et al. 2014, Roberts-Borsani et al. 2016, Stark et al. 2017, Endsley et al. 2021, Kashino et al. 2022, Matthee et al. 2022, Asada et al. 2022, Laporte et al. 2022, Williams et al. 2023, Rinaldi et al. 2023). Regardless of their redshifts, EELGs are characterized by very powerful UV-optical nebular emission lines, which are driven by elevated levels of star formation. EELGs at all redshifts share many of the same properties, which work together to drive their strong emission lines: they are typically low mass, metal poor galaxies with little dust and compact morphologies.

An example of an EELG spectrum is shown in Figure 1.1. This is a medium resolution spectra of the rest-frame optical part of the spectrum of a $z = 7.664$ galaxy presented in Schaerer et al. 2022. As expected of EELGs, this galaxy exhibits strong [OIII] emission, with a rest-frame Equivalent Width (EW) of EW([OIII]λ5007) $\approx$ 700Å, and includes several other strong emission lines, including the Balmer series, [OII], [NeIII], and HeI lines. While it is common for EELGs to have many strong emission lines, they are typically classified as EELGs based on the EW of only one or two of their emission lines (most commonly Hα and/or [OIII] + Hβ emission lines). Emission line EW (most commonly measured in Å) provides a measure of emission line strength relative to the underlying continuum emission, defined as

$$EW = \int \frac{F_l - F_c}{F_c} d\lambda \tag{1}$$

where F_c is the continuum emission and F_l is the line emission. There is no universal definition of what constitutes an EELG, with the required EW often varying by author and redshift. Generally,

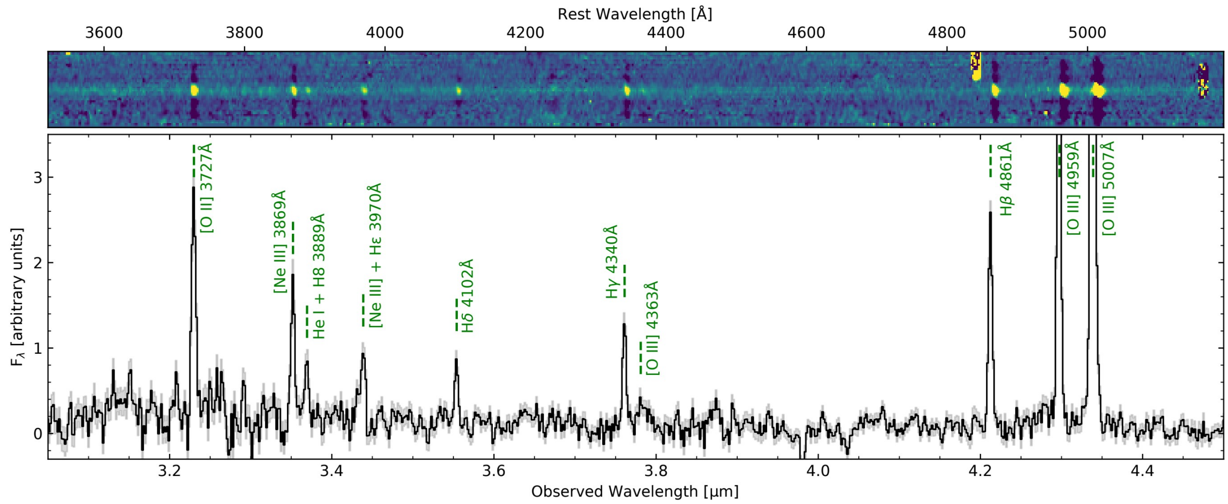

Figure 1.1: Figure 1 of Schaerer et al. 2022. A medium resolution NIRSpec spectrum of a $z \sim 8$ galaxy from the SMACS0723 ERO. This SED is representative of typical EELGs, with several strong emission lines including [OIII] + Hβ as well as other weaker lines.

galaxies with rest-frame EWs $\gtrsim 100$Å can be considered EELGs, however this often increases towards higher-redshift where galaxies become more star-forming and have generally higher EWs than at lower-redshift (e.g. Reddy et al. 2018, Matthee et al. 2022). For example, typical star-forming galaxies in the local Universe tend to have EWs $\lesssim 100$Å making EELGs quite rare in the local Universe (Cardamone et al. 2009). While rare, small numbers of EELGs with EWs up to $\sim 1000-2000$Å have been identified locally, including Green Peas, Purple Grapes, and Blueberries, named after their extreme colours in the Sloan Digital Sky Survey (e.g. Cardamone et al. 2009, Liu et al. 2022), as well as other compact star-forming galaxies (Izotov et al. 2021). However when moving to higher-redshifts, star-forming galaxies commonly have much higher EWs with typical values closer to several hundred Å by $z \sim 6$ (e.g. Endsley et al. 2023a, Endsley et al. 2023b), to the point where galaxies with EWs([OIII] + Hβ) less than 500Å are considered "weak" [OIII] + Hβ emitters by some authors (e.g. Endsley et al. 2023a). As discussed further in §3.5, we consider EELGs to be galaxies with EW([OIII] + Hβ) $\gtrsim 1000$Å and EW(Hα) $\gtrsim 500$Å.

1.2 Epoch of Reionization and Early Galaxies

One of the major motivations for searching and studying EELGs has to do with the role of star-forming galaxies in the epoch of reionization (EoR). The EoR marks an important point in the evolution of our Universe, being the time when Hydrogen in the intergalactic medium (IGM) was slowly transitioning from neutral to ionized. The process of Hydrogen reionization is summarized in Figure 1.2. Beginning at $z \sim 15$, the first stars and galaxies began to form and emit UV radiation that ionized the surrounding neutral Hydrogen. This created many ionized bubbles surrounding galaxies, which began to grow and overlap over time, eventually leading to an ionized IGM by $z \sim 5.5$ (e.g. Endsley et al. 2023b, McGreer et al. 2015). Much of our current knowledge of reionization comes from simulations and observations of the cosmic microwave background, with less information coming from observations of galaxies during the EoR. Thus, there remain many open questions regarding the process of reionization.

It has long been a goal of extragalactic astronomy to understand the sources responsible for reionization. To this end, there have been many searches dedicated to identifying and characterizing high-redshift galaxies. While these searches have identified many objects during the EoR, a detailed accounting of the sources responsible for reionization remains incomplete. Current estimates on the number densities of quasars and active galactic nuclei (AGN) at high-redshift show that while AGN may provide some contribution to reionization (e.g. Fujimoto et al. 2023), they are likely not responsible on their own (e.g. Adams et al. 2023). Because of this, it is currently presumed that strongly star-forming galaxies are the main drivers of Hydrogen reionization, specifically *faint* star-forming galaxies which appear to greatly outnumber more luminous galaxies in the EoR (e.g. Robertson et al. 2015, Stefanon et al. 2022). Included in this population of faint star-forming galaxies is EELGs, as many star-forming galaxies in the EoR have high EW emission lines. Additionally, emission line EW has been shown to anti-correlate with galaxy stellar mass, making lowest mass galaxies the strongest line emitters (e.g. Matthee et al. 2022, Onodera et al. 2020, Rinaldi et al. 2023). While not all star-forming galaxies can be classified as EELGs, they have been shown to be abundant at high-redshifts (Stark et al. 2013, Smit et al. 2014) and have properties that suggest they play an important role in reionization (e.g. Sun et al. 2022, Asada et al. 2022). As such, EELGs are a natural target when looking to study star-forming galaxies in the EoR.

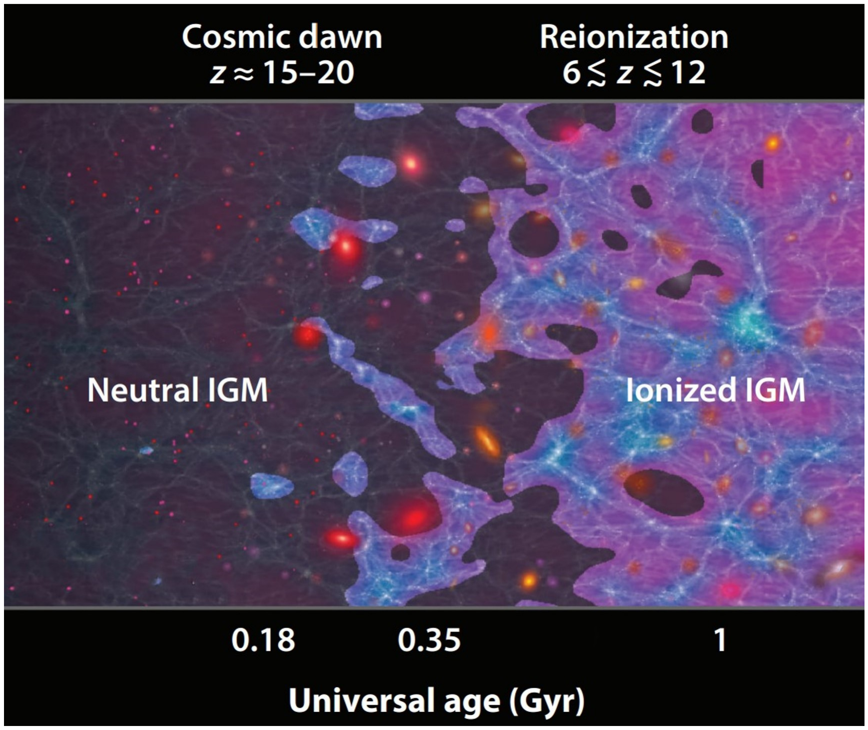

Figure 1.2: A portion of Figure 1 from Robertson 2022. An summary of reionization, showing the transition of the IGM from neutral to ionized over $z \sim 15 - 5.5$ driven by ionizing radiation from galaxies.

Additionally, high-redshift EELGs are interesting targets independent of their role in reionization. As reionization era objects, they are among the first generation of galaxies to form and evolve in our Universe. Studies of emission lines can provide a wealth of information regarding the state of the interstellar medium (ISM) in galaxies (e.g. Kewley et al. 2019), meaning EELGs can provide useful information on the evolution of early galaxies.

While many studies target high-redshift EELGs, it is also important to note that lower-redshift EELGs can provide useful insights on the high-redshift population. This includes EELGs in the local Universe (as discussed in §1.1), as well as EELGs at intermediate-redshifts. As mentioned above, EELGs share many of the same properties regardless of their redshifts and low(er)-redshift EELGs have been shown to have similar properties to high-redshift star-forming galaxies (e.g. Rhoads et al. 2023, Schaerer et al. 2022, Izotov et al. 2021). Thus, these local/lower-redshift EELGs can serve as analogues to not only the high-redshift population of EELGs but also the population of normal star-forming galaxies at high-redshift. This can be very useful, since lower-redshift analogues can be in many ways easier to study than their higher-redshift counterparts. These lower-redshift analogues have provided useful information on the high-redshift population in the past, and will likely continue to do so in the future (e.g. Tang et al. 2022, Mingozzi et al. 2022, Rhoads et al. 2023).

1.3 Observations of EELGs

While EELGs have been studied for years, reaching a full understanding of these objects has been prevented due to several observational constraints. This is especially true for the highest-redshift EELGs during the EoR, which were many times too faint to be fully characterized by existing facilities. This has begun to change within the past year following the successful launch and commissioning of the James Webb Space Telescope (JWST, Rigby et al. 2023). Owing to JWST's sensitivity and wavelength coverage, it is now possible to more fully characterize the population of EELGs up to $z \sim 9$, deep into the EoR. Early JWST studies have already begun to yield a wide variety of interesting results on EELGs at many redshifts.

So far, there have been several hundred high-redshift star-forming galaxies discovered by JWST, which are providing the first look at the population of low mass galaxies at those redshifts. Included in these samples are many EELGs, some with EW > 1000Å for [OIII] + Hβ and Hα, up to $z \sim 9$, which provides confirmation that EELGs are common in the high-redshift Universe (e.g. Matthee et al. 2022, Kashino et al. 2022, Williams et al. 2023, Rinaldi et al. 2023, Laporte et al. 2022). Analysing the physical properties of these EELGs reveals that they are generally low mass systems that have young stellar ages (≤ 30 Myr) and little dust attenuation as evidenced by blue continua (Endsley et al. 2023a, Saxena et al. 2023, Mascia et al. 2023). Interestingly, there have also been several EELGs that have been found to have larger ages (closer to ~ 150Myr) as well as very dusty galaxies which appear to host obscured star formation (e.g. Laporte et al. 2022, Endsley et al. 2023a). Additionally, detailed spectroscopic observations from JWST have allowed for several studies on the physical conditions of the ISM of high-redshift EELGs. These studies find that high-redshift star-forming galaxies have generally high ionization parameters, low metallicities, and similar line ratios to what is seen in low(er)-redshift EELGs, which continues to show that low-redshift EELGs provide good analogues to the high-redshift population of star forming galaxies (Trump et al. 2022, Taylor et al. 2022, Matthee et al. 2022).

Other work has begun detailed investigations of the role of star-forming galaxies in reionization. This includes observations of Lyman α Emitters (LAE), which are star-forming galaxies/EELGs which also have Lyα emission. LAEs have been observed at lower-redshifts, but are rare in the EoR since the Lyα line is strongly attenuated by the IGM. Some samples of LAEs have EW(Lyα) of up to ~ 350Å (e.g. Saxena et al. 2023) and can provide valuable insights into how Hydrogen ionizing radiation escapes from galaxies. Additionally, some work has focused on Lyman Continuum (LyC) escape fractions, f_{esc}(LyC), at high-redshifts, which describes the fraction of LyC radiation that is able to escape from the ISM and contribute to reionization. The f_{esc}(LyC) of star-forming galaxies is essential to assess their contribution to reionization, but is impossible to directly measure at $z \gtrsim 4$ due to absorption from the IGM. Much of this work has focused on searching for indirect indicators for f_{esc}(LyC), while early estimates on f_{esc}(LyC) shows that, on average, star-forming galaxies have f_{esc}(LyC) high enough to be responsible for reionization (e.g. Saxena et al. 2023, Mascia et al. 2023, Atek et al. 2023) . Finally, many works have measured the Hydrogen ionizing photon production efficiency (ξ_{ion}) of high-redshift galaxies, defined as

$$\xi_{ion} = 7.35 \times 10^{11} \frac{L(H\alpha)}{L(UV)} \tag{2}$$

where $L(H\alpha)$ is the Hα luminosity, which provides a measure of the intrinsic Hydrogen ionizing photon production in the galaxy, and $L(UV)$ is the UV luminosity measured at 1500Å, which provides a measure of the production of photons which are not energetic enough to ionize Hydrogen (e.g. Nanayakkara et al. 2020). Overall, ξ_{ion} provides a measure of the amount of radiation a galaxy is producing that is able to contribute to reionization, and is a critical to assess the role of galaxies to reionization, especially when combined with measures of f_{esc}(LyC) (e.g. Saxena et al.

2023, Atek et al. 2023). These studies have shown that EELGs in the EoR typically have high ξ_{ion} values, as would be expected if these sources are responsible for reionization (e.g. Sun et al. 2022, Asada et al. 2022). Combining the results of these early studies, the emergent picture is that star-forming galaxies such as EELGs have properties consistent with them being responsible for reionization. While these early results are encouraging, a systematic accounting of reionization era sources remains incomplete. In order to fully assess the role of galaxies in reionization, large samples of faint galaxies with high completeness fractions are required, which remains to be done. As will be discussed in the next section, finding and characterizing EELGs provides a convenient way to systematically study galaxies in the EoR, since EELGs represent the extreme star-forming galaxies which are thought to be responsible for reionization.

1.4 The Power of Medium-Band Photometry

Many of the searches for EELGs select samples using either broad-band photometry (e.g. Stark et al. 2013, Onodera et al. 2020) or wide field slitless spectroscopy (WFSS, e.g. Maseda et al. 2014, Maseda et al. 2018, Kashino et al. 2022, Boyett et al. 2022). While these kinds of observations have produced many important results, there are challenges and biases associated with each technique. Broad-band filters can have very large bandwidths (particularly the redder NIRCam filters, which have bandwidths of up to $\sim 1\mu$m), which does not provide very detailed spectral information on galaxy SEDs. This can make it challenging to accurately determine redshifts and other properties in certain cases, as well as create issues with sample contamination when there are degeneracies in broad-band photometry (further discussed below). While WFSS is able to provide significantly more spectral information by obtaining a spectra of many objects at once, it suffers from its own issues as well. This includes overlapping source contamination which can make it challenging to properly disentangle the extracted spectra, particularly for faint objects.

While less common, medium-band photometry offers a convenient solution to these problems. The smaller bandwidths of the medium-bands offers increased spectral resolution compared to the broad-bands, which provides more detailed information and improves estimates of galaxy properties (e.g. Roberts-Borsani et al. 2021, Sarrouh et al. in preparation). Additionally, medium-band imaging is free of many of the challenges associated with WFSS observations, and can reach greater depths per unit exposure time than WFSS. Due to these differences, the medium-bands offer many advantages over more conventional methods at studying the general galaxy population, and are a particularly powerful tool in the search for EELGs (Terao et al. 2022, Gupta et al. 2023, Laporte et al. 2022, Williams et al. 2023).

A simple and effective way of searching for EELGs using medium-band photometry is by using colour selections. These colour selections target the extreme colours produced by extreme emission lines, which can reach medium-band colours > 2 mag relative to the neighbouring filters. This is exemplified in Figure 1.3, which shows both simulated and real medium-band colours for galaxies in the JWST Extragalactic Medium-band Survey (JEMS) programs, one of the few JWST programs to have extensively utilized the medium-bands aboard NIRCam. The colour in Figure 1.3 is from two medium-bands at $\lambda \sim 4\mu$m, which have extreme colours driven by several different emission lines, including Hα, [OIII] + Hβ, and Paschen lines. This clearly demonstrates the effect of emission lines on medium-band colours, and highlights how they can then be used to select EELGs over a very large range of redshifts by targeting extreme colours. It is worthwhile to point out that while it is possible to search for extreme colours/flux excesses using broad-band photometry, medium-band photometry is much more efficient. This is partly because of the increased spectral resolution of the medium-bands (as discussed above), but also because the smaller bandwidths of the medium-bands lead to significantly larger flux excesses than the broad-bands (as has been noted in other works, e.g. McKinney et al. 2023). This makes emission lines easier to identify and distinguish from other spectral features (such as spectral breaks) with medium-bands, and allows the medium-bands to target lower EW systems than the broad-bands.

One of the advantages of using medium-band colour selections to target EELGs is that they can select galaxies based on emission line flux, with no reliance on continuum emission. This is in contrast to many of the typically used selection criteria, where a Lyman break is incorporated into the selection. The Lyman break is caused by large amounts of neutral Hydrogen in the IGM

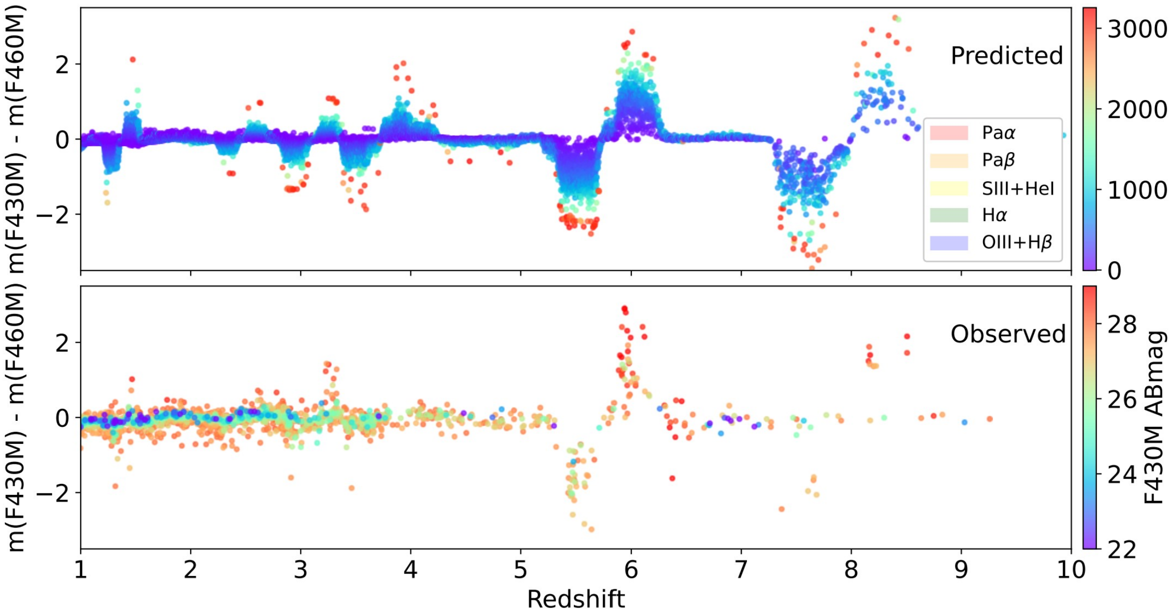

Figure 1.3: A portion of Figure 5 in Williams et al. (2023). Plots the $F430M - F460M$ colour as a function of redshift for simulated galaxies (top) and real galaxies in JEMS (bottom) this highlights the extreme colours driven by EELGs in the medium-bands, and how medium-band colour selections can be used to identify EELGs over a wide range of redshifts.

absorbing light bluewards of $\lambda = 1216$Å in the rest-frame, creating a sharp spectral break where galaxies appear to "drop out" of observations. While there have been many of these Lyman break galaxies (nicknamed the "drop outs") identified in imaging and spectroscopic data, these samples are heavily biased towards galaxies with strong enough continuum emission to produce a detectable Lyman break. Thus, many of the commonly-used selection criteria will fail to select very faint galaxies for which a Lyman break cannot be observed.

Therein lies the power of medium-band colour selections: unlike the Lyman break technique, medium-band colour selections do not require robust detections (high signal to noise ratios) in the rest-frame UV-optical continuum. Instead, they target *flux excesses* driven by strong emission lines, which are independent of underlying continuum emission. This allows the medium-band colour selections to identify ultra-faint, "emission line only" galaxies, which are too faint to be detected through their continuum emission alone. This population of very faint galaxies has been shown to exist in the EoR and play an important role in reionization (e.g. Endsley et al. 2022, Endsley et al.

2023b, Atek et al. 2023), yet are challenging to detect using typical selection criteria. However, faint and low-mass EELGs often have strong emission lines, allowing them to be easily selected using medium-band colour cuts.

Not only this, but medium-band imaging can provide a unique window into dusty star-forming galaxies at high-redshifts. While most EELGs have very little dust, there is increasing evidence for a population dusty EELGs at high-redshifts (e.g. Endsley et al. 2023a). These galaxies have the powerful emission lines characteristic of EELGs, but their large amounts of dust make their continuum fluxes very red, sometimes so much that the fluxes redwards of the of $\lambda = 1216$Å are far too faint to produce a noticeable Lyman break. Not only can these dusty star-forming galaxies be important for studying obscured star formation in the early Universe, but their broad-band photometry has been shown to be degenerate with that of very high-redshift ($z > 10$) Lyman break galaxies (e.g. Arrabal Haro et al. 2023, Zavala et al. 2023). An example of this is provided in Figure 1.4, CEERS-93316.

CEERS-93316 was originally selected as a candidate $z \approx 16$ galaxy by using 7 (mainly broad) band filters (F115W, F150W, F200W, F277W, F356W, F410M, F444W), but was revealed to be a $z \approx 4.9$ dusty star-forming galaxy when observed by NIRSpec. Looking at the spectrum, it is clear how CEERS-93316 was mistaken for a high-redshift galaxy: strong Hα emission boosted the fluxes in three filters (F356W, F410M, F444W), [OIII] + Hβ boosted the flux in F277W, while its red continuum fluxes led to a very faint detection in F200W and non-detections in F150W, F115W, and bluer filters observed with the Hubble Space Telescope (HST). This photometry is very similar to what would be expected of a $z \approx 16$ dropout which would have continuum emission in F277W, F356W, F410M, F444W, a Lyman break in F200W, and then no detections in bluer filters. Adding so much as a single medium-band to these observations would have broken this degeneracy, which highlights the value of using medium-band photometry in imaging surveys, as medium-band photometry/colour selections are able to easily reveal the true nature of objects such as CEERS-93316, without spectroscopy.

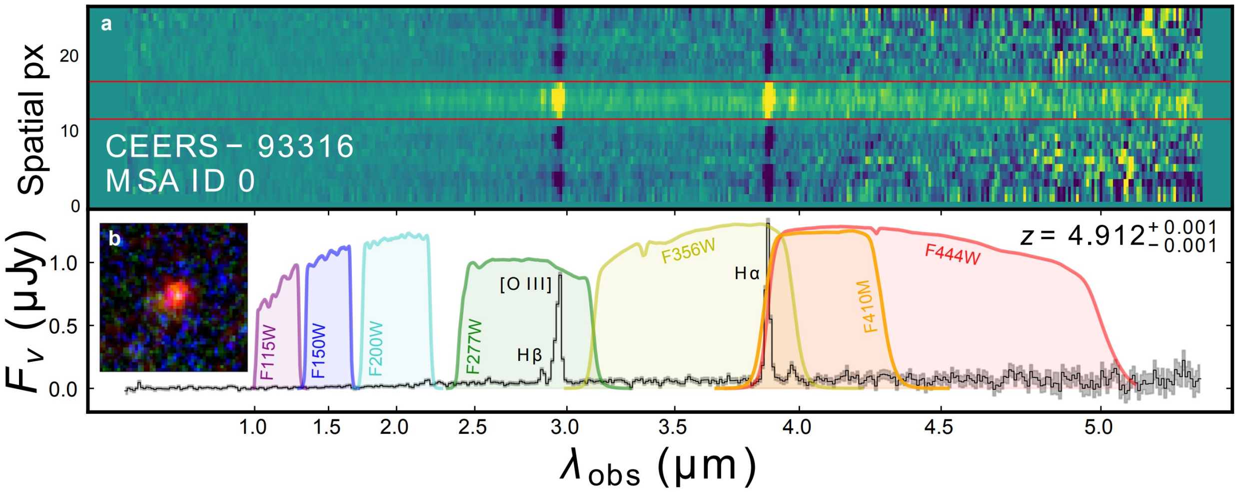

Figure 1.4: Figure 3 of Arrabal Haro et al. 2023. The spectrum of CEERS-93316, a dusty star-forming galaxy which mimicked the photometry of a $z \sim 16$ drop-out. This highlights the advantages of using medium-band photometry, which can easily identify galaxies such as these.

1.5 Motivation and Outline

Given the wealth of information that can be gained by studying EELGs, this work focuses on selecting EELGs both during the EoR as well as analogues at lower-redshifts by exploiting the power of medium-band photometry to identify EELGs. Specifically, we use the suite of medium-band filters aboard JWST/NIRCam to select EELGs using a set of colour cuts that target galaxies with strong [OIII] + Hβ and Hα emission. We discuss the observations used in this work in §2, and the colour selections in §3. These colour cuts produce a sample of 118 EELGs over $1.7 \lesssim z \lesssim 6.7$, which are characterized by strong [OIII] + Hβ and Hα emission. The sample is discussed in §4, including their physical properties and EWs. Finally, we test the effectiveness of these colour selections in §5, by using NIRSpec spectroscopy of a sub sample of our EELGs. Portions of this work do also appear in a peer-reviewed publication in the Astrophysical Journal Letters (Withers et al. (2023)).

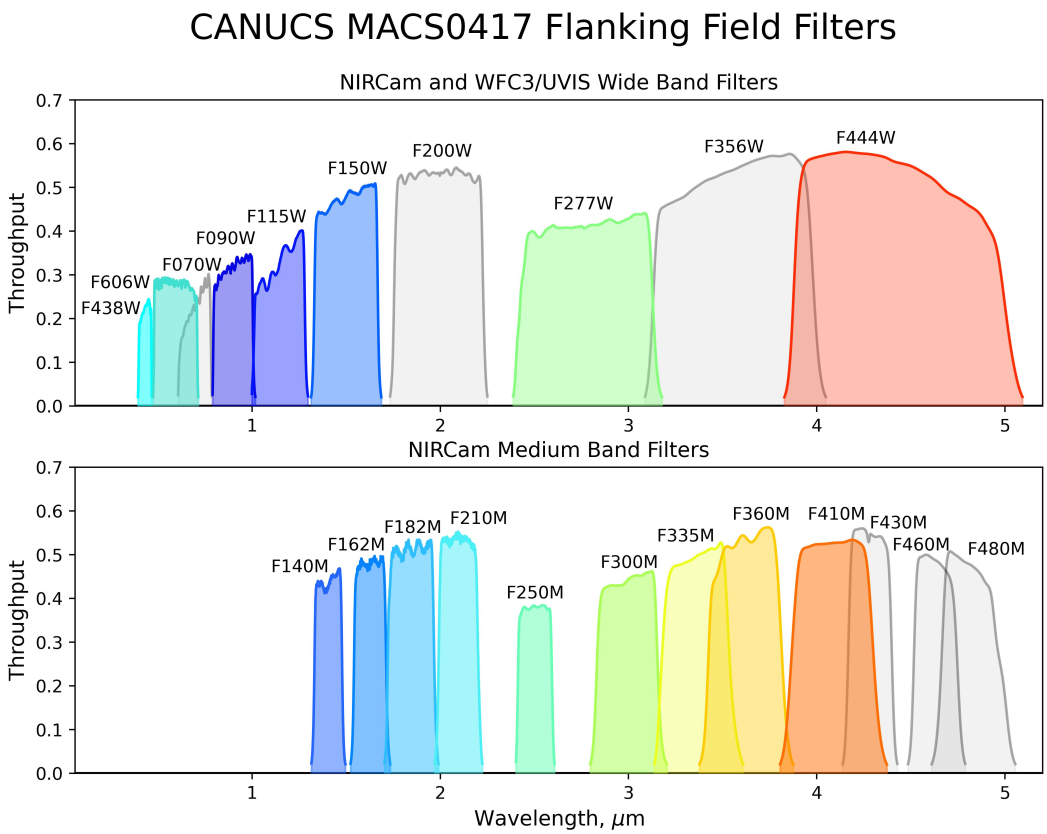

Figure 2.1: The filter throughput curves (including the total system throughput's and averaged over all NIRCam detectors) used in the CANUCS NIRCam observations (colourful curves) of the field parallel to MACS0417. The top panel shows the five NIRCam wide band filters (F090W, F115W, F150W, F277W, and F444W) as well as the two WFC3/UVIS filters (F438W and F606W), and the bottom panel shows the nine NIRCam medium-band filters (F140M, F162M, F182M, F210M, F250M, F300M, F335M, F360M, F410M). Additionally, the only other NIRCam filters that were not used in CANUCS are plotted in grey (two wide bands, three medium bands). The filter throughput for the NIRCam filters are obtained from https://jwst-docs.stsci.edu/jwst-near-infrared-camera/nircam-instrumentation/nircam-filters and the WFC3/UVIS filter throughput curves are obtained from https://www.stsci.edu/hst/instrumentation/wfc3/performance/throughputs.

2 Observations

2.1 Photometry

This work uses imaging data from the JWST Near Infrared Camera (NIRCam, Rieke et al. 2023) instrument, obtained as part of the CAnadian NIRISS Unbiased Cluster Survey (CANUCS, Willott et al. 2022, GTO ID 1208). CANUCS observations include several pointings which provide deep

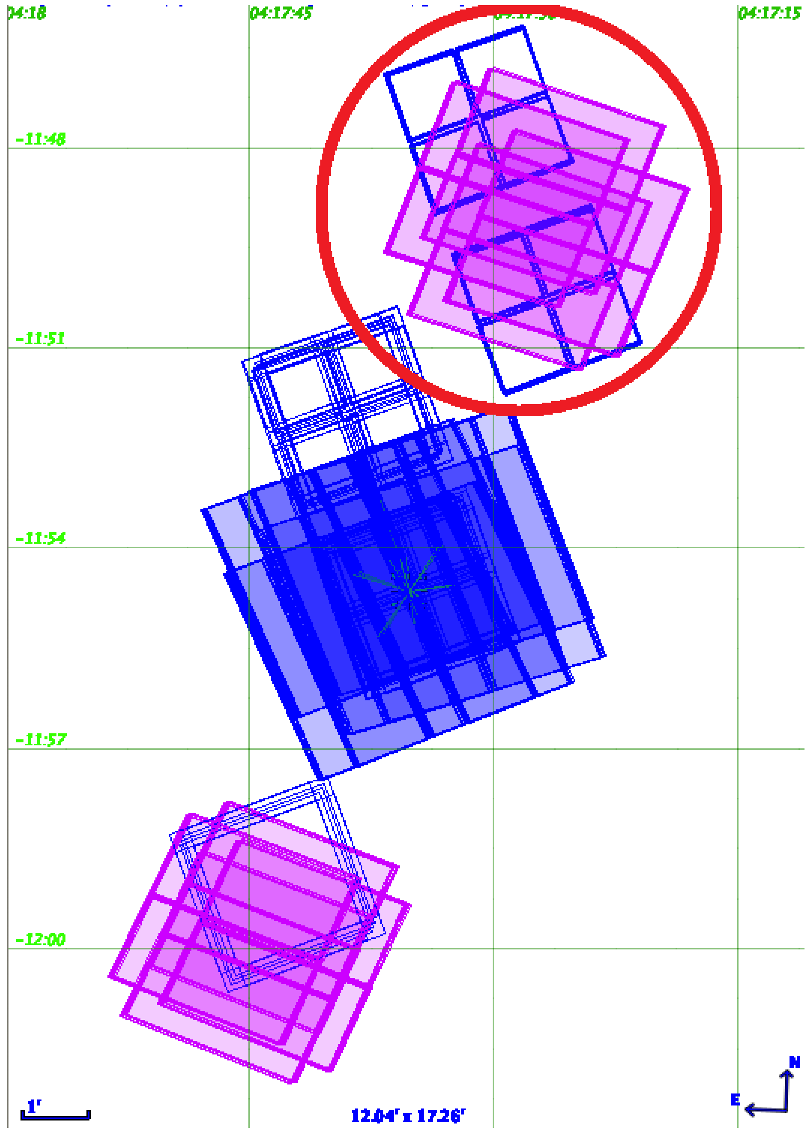

Figure 2.2: Summary of the CANUCS observations of the MACS 0417 field. The field used for this work is at the top, highlighted in the red circle, where the blue outline represents the NIRCam coverage and the pink outline represents the WFC3/UIVS coverage. There is a $\sim 70\%$ overlap of the NIRCam and WFC3/UVIS fields. Image is taken from https://niriss.github.io/fields.html.

(~ 28.9 mag in medium-bands, ~ 29.4 mag in wide bands to 5σ for point sources) NIRCam imaging in five broad (F090W, F115W, F150W, F277W, F444W) and nine medium-band (F140M, F162M, F182M, F210M, F250M, F300M, F335M, F360M, F410M) filters (see Figure 2.1, Table 1). These observations use 14 out of the 20 medium- and broad-band filters available on NIRCam, missing only three broad-band and three medium-band filters. This is reflected in Figure 2.1 which shows the filter throughput curves (including the total system throughput's and averaged over all NIRCam detectors) of the 14 broad- (top) and medium-band (bottom) filters used in CANUCS in colour as well as the six additional filters available on NIRCam in grey. The extensive use of NIRCam medium-bands in the flanking fields makes CANUCS unique among current JWST observations, and provides an ideal data set to search for EELGs using medium-band colour selections over a wide range of redshifts.

This work focuses on observations of the first of the five CANUCS fields, a field adjacent to massive galaxy cluster MACS J0417.5-1154 (RA = $04:17:35.1485$ and Dec = $-11:54':38.44$). This field is shown in Figure 2.2 which we call the NIRCam flanking field (top right), along with the cluster field (middle) and NIRISS flanking field (bottom). Only the NIRCam flanking field is used in this work, since it is the only field to include extensive medium band imaging. These NIRCam observations are obtained in a single NIRCam pointing using modules A and B covering an area of 9.7 arcmin^2, with a colour image of the NIRCam observations shown in Figures 2.3 and 2.4. Additionally, $\sim 70\%$ of the NIRCam flanking field was observed by HST using two filters (F438W and F606W) onboard the Wide Field Camera 3/UVIS instrument to depths of ~ 28.4 mag at 5σ for point sources (Program ID 16667, PI M. Bradac). Together, the JWST and HST observations provide a wavelength coverage of $\lambda \sim 0.4-5\mu$m in 16 filters, shown in Figure 2.1 with information on each of the filters in Table 1. Magnification from gravitational lensing due to the massive galaxy cluster MACS0417 is negligible in this field, and is thus neglected in this analysis.

2.2 Spectroscopy

In addition to the imaging data, CANUCS provides follow-up spectroscopy with the Near Infrared Spectrograph (NIRSpec, Böker et al. 2023). We obtained follow-up spectroscopy of a subset of the EELGs used in this work (discussed in §5.1). The spectra were acquired with NIRSpec in multi-object spectroscopy (MOS) mode using $\sim$ 3ks integration times, and using the prism which provides low-resolution spectroscopy ($R \sim 100$) over $\lambda \sim 0.6-5.3\mu$m.

Filter Col. 1	Instrument Col. 2	Pivot Wavelength (μm) Col. 3	Bandwidth (μm) Col. 4	5σ Depth Col. 5
F438W	WFC3/UVIS	0.434	0.0615	28.06
F606W	WFC3/UVIS	0.589	0.218	28.76
F090W	NIRCam	0.901	0.194	29.11
F115W	NIRCam	1.154	0.225	29.19
F140M	NIRCam	1.404	0.142	28.47
F150W	NIRCam	1.501	0.318	29.34
F162M	NIRCam	1.626	0.168	28.56
F182M	NIRCam	1.845	0.238	29.24
F210M	NIRCam	2.093	0.205	28.95
F250M	NIRCam	2.503	0.181	28.42
F277W	NIRCam	2.786	0.672	29.86
F300M	NIRCam	2.996	0.318	28.90
F335M	NIRCam	3.365	0.347	29.35
F360M	NIRCam	3.621	0.372	29.33
F410M	NIRCam	4.092	0.436	29.25
F444W	NIRCam	4.421	1.024	29.42

Table 1: Information on the 16 filters used to observe the MACS0417 parallel field. This includes the filter name (Col. 1), the instrument (Col. 2), pivot wavelength (Col. 3), filter bandwidth (Col. 4), and the 5σ, point-source depth in AB magnitudes (Col. 5). Values listed in Col. 3 and 4 for NIRCam filters were obtained from https://jwst-docs.stsci.edu/jwst-near-infrared-camera/nircam-instrumentation/nircam-filters and from https://hst-docs.stsci.edu/wfc3ihb/chapter-6-uvis-imaging-with-wfc3/6-5-uvis-spectral-elements for WFC3/UVIS filters.

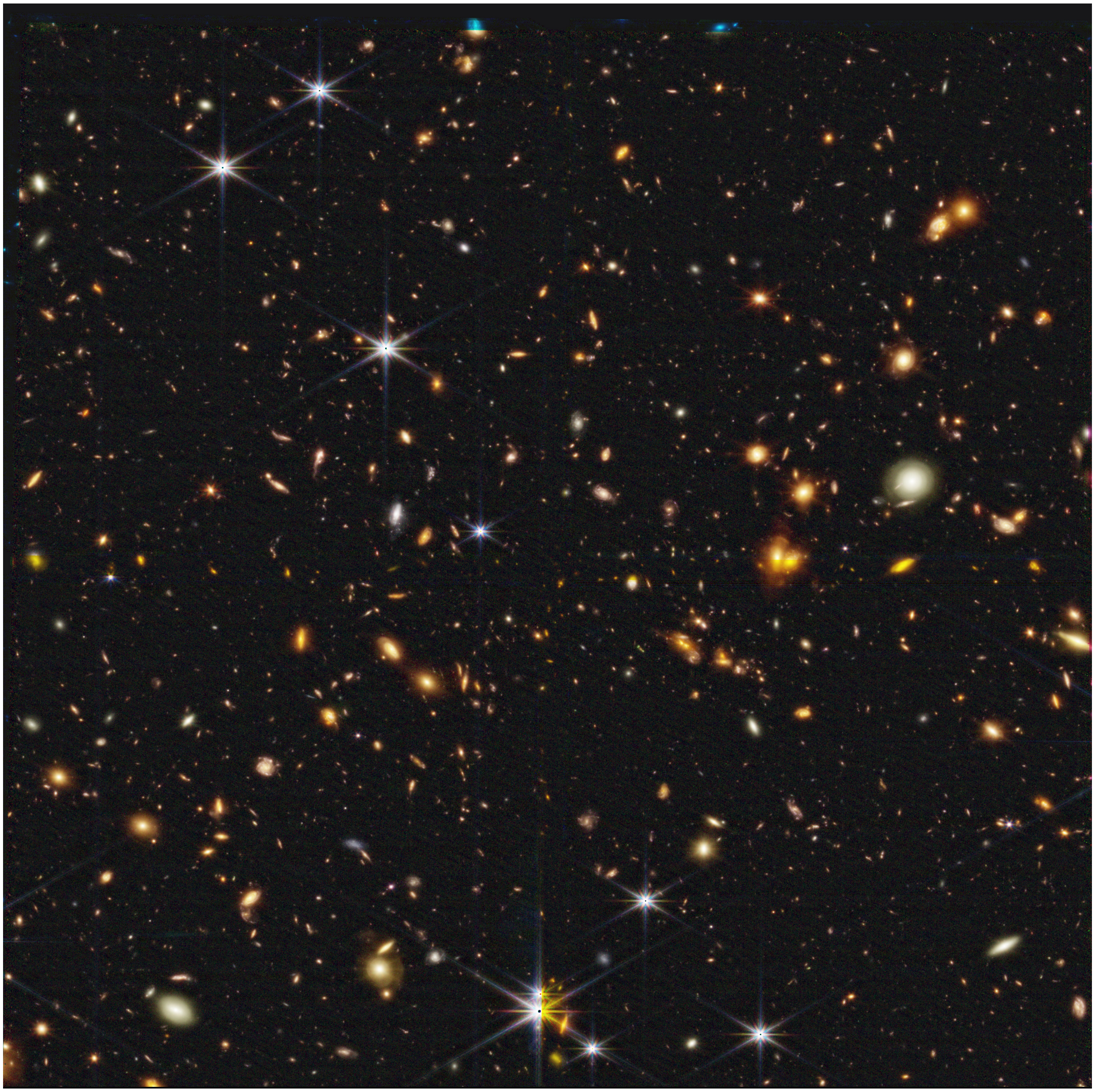

Figure 2.3: A colour image of the MACS 0417 flanking field from CANUCS. NIRCam consists of two $2.2' \times 2.2'$ modules separated by $5.1'$, which are called Module A and B. This figure shows Module A, Module B is shown in Figure 2.4. Blue channel: average of F090W, F115W, F150W; Green channel: average of F182M, F210M, F250M, F300M; Red channel: average of F335M, F360M, F410M.

Figure 2.4: A colour image of the MACS 0417 flanking field from CANUCS. NIRCam consists of two $2.2' \times 2.2'$ modules separated by $5.1'$, which are called Module A and B. This figure shows Module B, Module A is shown in Figure 2.3. Blue channel: average of F090W, F115W, F150W; Green channel: average of F182M, F210M, F250M, F300M; Red channel: average of F335M, F360M, F410M.

3 Synthetic Observations & Colour Selections

Before EELGs could be selected in CANUCS imaging data, it was necessary to create a set of colour cuts that were able to efficiently select EELGs. This project began several months before any JWST data was available, thus we had to create synthetic CANUCS observations in order to define the colour cuts. These colour selections were then applied to CANUCS data when they became available in October 2023. The process of creating and testing the synthetic observations is described below.

3.1 Models of Extreme Emission Line Galaxies

The first step in this process is to obtain a set of galaxy Spectral Energy Distributions (SEDs) that are representative of the population of EELGs to determine their colours. To this end, a set of stellar population synthesis (SPS) models were selected which are able to accurately model the spectra of high-redshift EELGs. Two sets of SPS models are used in this work. Both are created using the `Yggdrasil` SPS code (Zackrisson et al. 2011), which is designed to model EELGs by accounting for the strong nebular emission that powers emission lines in EELGs. The first set of models (refereed to simply as the `Yggdrasil` models) are a set of "toy" models that make simple assumptions about galaxy properties in order to generate SEDs. Of the set of publicly-available `Yggdrasil` models, we select a subset of ~ 90 SEDs which all have properties common of EELGs: a Kroupa (2001) initial mass function (IMF) and four star formation histories (SFHs, instantaneous burst and constant star formation rates with timescales of 10Myr, 30Myr, and 100Myr). Each SFH had one of three metallicities ($Z = 0.0004, 0.004, 0.008$) and was "observed" at various ages ($0.01 - 9.1$ Myr after star formation began).

In addition to the `Yggdrasil` models, the `LYCAN` SPS models (Zackrisson et al. 2017) were also used in this work. The `LYCAN` models are created using the `Yggdrasil` SPS code, however they are models of $z \approx 7$ galaxies drawn from four independent cosmological simulations (Gnedin 2014, Paardekooper et al. 2015, Finlator et al. 2013, and Shimizu et al. 2014). Unlike the `Yggdrasil`

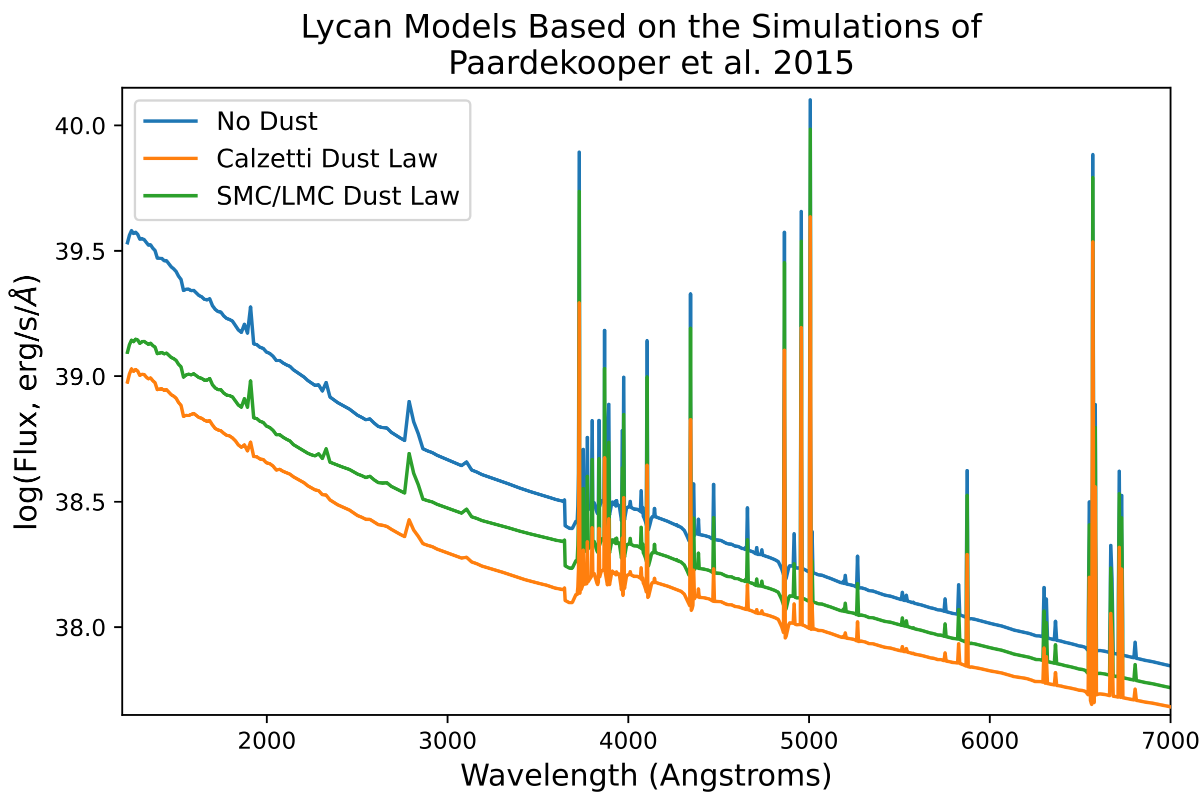

Figure 3.1: Three example SEDs from the LYCAN SPS code. All of the models are based on the same galaxy from the simulations of Paardekooper et al. 2015, either no dust extinction or dust extinction defined by the extinction curves of Calzetti 2001 or Pei 1992.

models, the LYCAN models do not rely on simplistic assumptions about galaxy SFH and metallicity that were required for the Yggdrasil models. Instead, information on galaxy SFH, metallicity, and dust attenuation were taken from the simulations and input into the Yggdrasil SPS code. Of the hundreds of publicly available *LYCAN* models, 181 are used in this work. SEDs were selected to cover a wide range of parameter space with different metallicities ($0.0002 < Z < 0.01$), amounts of dust extinction ($0 < A_V < 0.9$) dust laws (Calzetti 2001, Pei 1992), and included galaxies from all four cosmological simulations.

Examples of three of the LYCAN SEDs used in this work are shown in Figure 3.1. While all the SEDs described in this section are designed to model the SEDs of high-redshift EELGs, the results can be safely extended down to lower-redshifts since EELGs have many of the same properties regardless of their redshifts (§1.1).

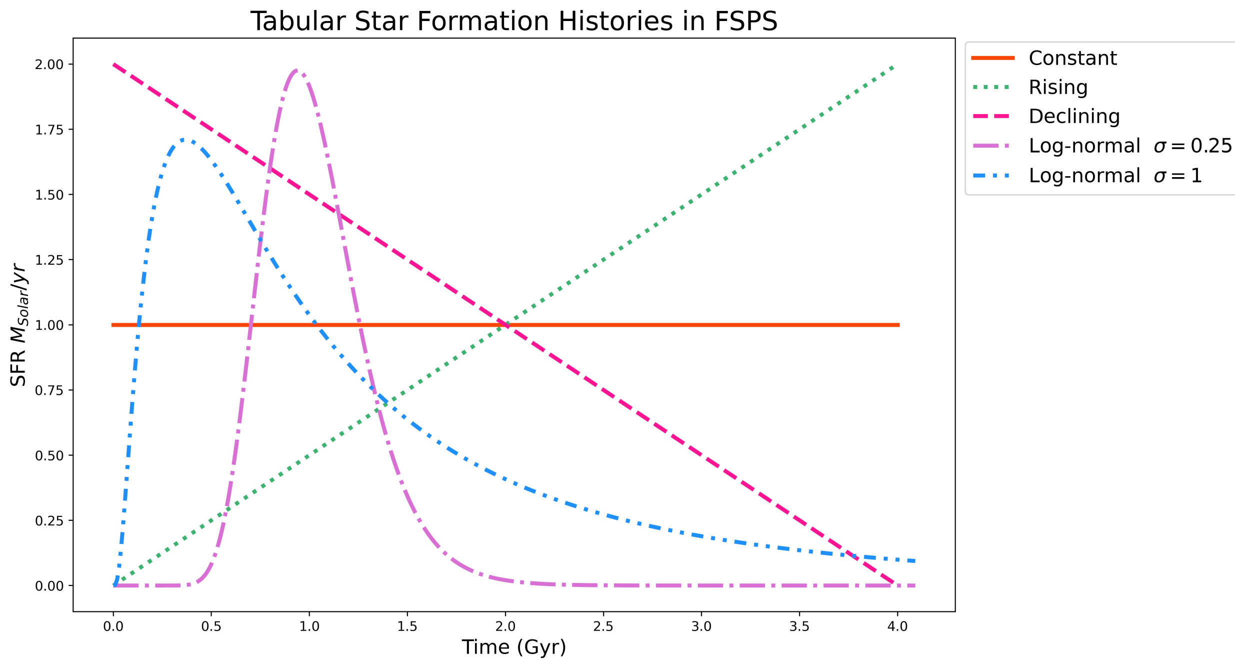

Figure 3.2: Five of the SFHs used to model create synthetic SEDs of other galaxy populations with `FSPS`. These are all tabulated SFHs that were manually defined and then input into `FSPS`. Not included in this plot are two SFHs which are defaults in `FSPS`, a burst-only SFH and three-component SFH.

3.2 Models of Other Galaxy Populations

The NIRCam observations used in this work will detect many types of galaxies at a variety of redshifts. These include EELGs, however, EELGs will be significantly outnumbered by other types of galaxies. These other populations can also have extreme colours which may mimic the signatures of EELGs and be selected by the colour cuts as well. Thus, the colours of other galaxy populations at various redshifts must also be determined in order to search for any contaminants and minimize these effects on the colour selections. This was done by creating synthetic observations of SEDs of a variety of galaxies, including old/passive galaxies, and less extreme star-forming galaxies. The models were created using the `Flexible Stellar Population Synthesis (FSPS)` code (Conroy et al. 2009, Conroy & Gunn 2010, specifically the `python FSPS` package), which creates synthetic SEDs for a wide range of input parameters including SFH, age, metallicity, and dust attenuation.

Several sets of input parameters were chosen to create the low-redshift SEDs. The different models all have the same metallicity ($Z = Z_\odot$) since this parameter had the smallest effect on the final SEDs. In contrast, the SFH and amount of dust attenuation had the largest effect on galaxy SEDs, thus these two parameters were varied. Seven different SFHs were used, five of which are summarized in Figure 3.2. These are all tabulated SFHs manually input into `FSPS`, including constant, rising, declining SFHs and two kinds of log-normal SFHs. In addition to those five, there are two additional SFHs used which are the default SFHs programmed into `FSPS`. One was a single-burst SFH, while the other is a three-component SFH including a burst component, constant component, and tau component of the form

$$SFR(t) \propto e^{-t/\tau} \tag{3}$$

where τ is the e-folding timescale of the SFH (we used $\tau = 1$Gyr), and SFR is the star formation rate. The dust attenuation used in each case is either no dust or $A_V = 0.6$, modelled using a Calzetti 2001 dust law. In total, there were ten different types of SEDs created each with a different combination of SFH and dust, summarized in Table 2. For each of the ten combinations of input parameters, the FSPS code was used to create 41 SEDs over 0.01 to 4 Gyr after the beginning of star formation. In total, this produced 410 low-redshift SEDs. Four examples of these SEDs are shown in Figure 3.3, which include two star-forming galaxies and two passive galaxies.

3.3 Galaxy Colours

Galaxy colours were determined for each of the model galaxies by redshifting each SED and calculating their synthetic magnitudes in each of the CANUCS NIRCam filters. These calculations were carried out as follows. In order to compute synthetic magnitudes, the integrated flux density, F_ν, of an SED at redshift z in the desired filter is required. This is defined as

$$F_\nu = \int_{\Delta\nu} \frac{f(\nu)t(\nu)}{\int_0^\infty t(\nu)d\nu} d\nu \tag{4}$$

for an SED with flux density $f(\nu)$ in a filter with throughput curve of $t(\nu)$. The integral in the

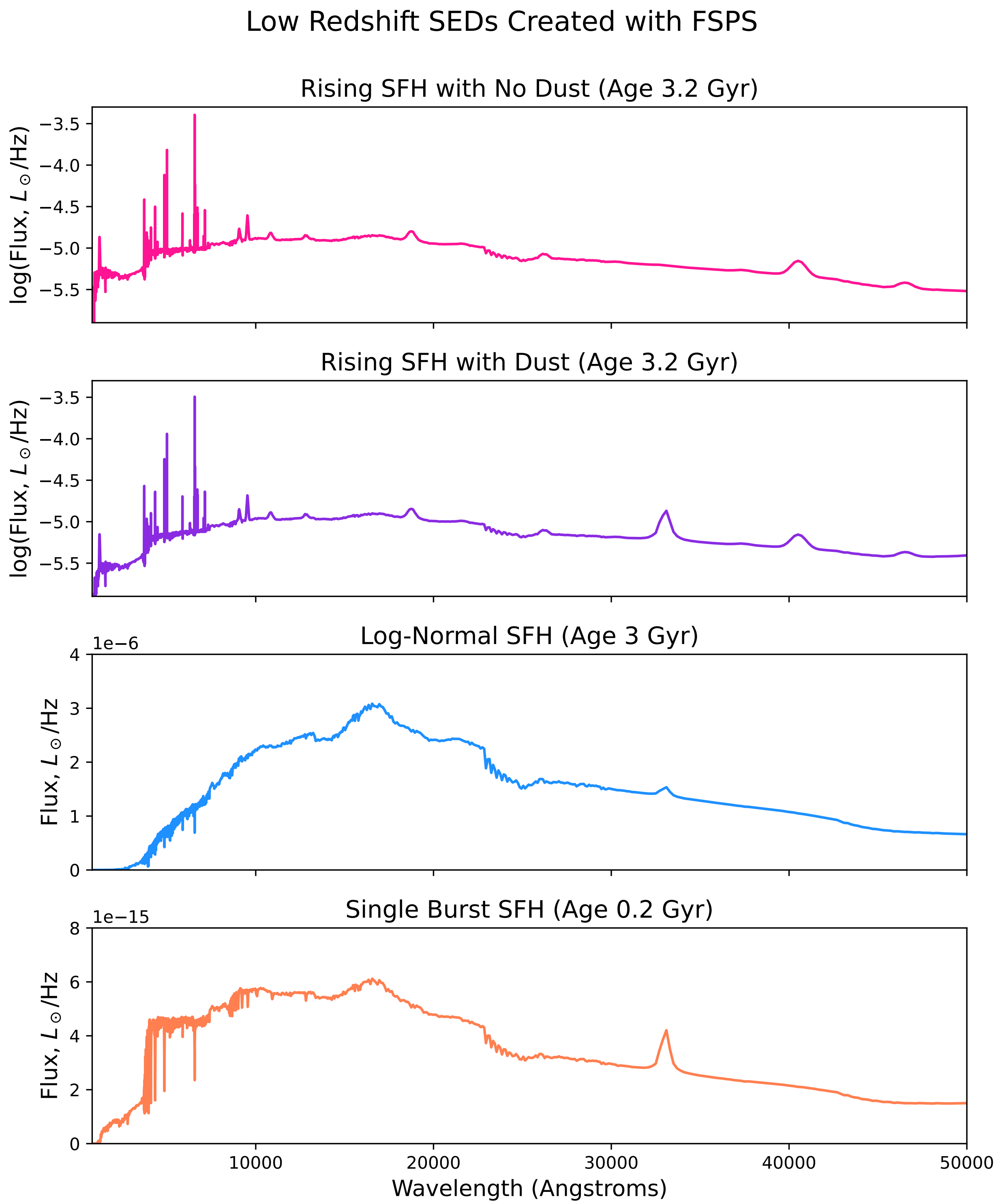

Figure 3.3: Four examples of the SEDs of non-EELG galaxy populations from the FSPS code, in the rest-frame. The top two panels are examples of regular star-forming galaxies (which is plotted in log flux units) and the bottom two panels are examples of passive galaxies (which is plotted in linear flux units).

Number Col. 1	Star Formation History Col. 2	Dust (A_V) Col. 3
1	Three-Component	0.6
2	Burst-Only	0.6
3	Constant	0.6
4	Rising	0.6
5	Declining	0.6
6	Log-Normal $\sigma = 0.25$	0.6
7	Log-Normal $\sigma = 1$	0.6
8	Three-Component	0
9	Constant	0
10	Rising	0

Table 2: Parameters used when creating synthetic SEDs of other galaxy populations with `FSPS`. Ten different combinations (Col. 1) of SFH (Col. 2) and dust extinction (Col. 3) were used to generate the SEDs.

denominator is to normalize the filter throughput curve $t(\nu)$ such that $\int_{\Delta\nu} t(\nu)d\nu = 1$. The filter throughput curves were obtained online from the NIRCam and WFC3 documentation (see the caption in Figure 2.1), and then the normalization for each filter was computed to be used in Eq. 4. Additionally, in order to be used in Eq. 4, $f(\nu)$ was interpolated to match the wavelength resolution of $t(\nu)$ using flux conserving interpolation.

Values for $f(\nu)$ were obtained from the SEDs described in §3.1 and 3.2. These were originally given in the rest-frame, and needed to be redshifted in order to be used in Eq. 4. This was done by multiplying the rest frame wavelengths by a factor of $1+z$, and by converting the flux into the appropriate units by dividing by $4\pi D_L$, where D_L is the luminosity distance defined as

$$D_L = \frac{c}{H_0} \times \int_0^z \frac{1}{\sqrt{\Omega_M(1+z')^3 + \Omega_k(1+z')^2 + \Omega_\Lambda}} dz' \tag{5}$$

where we use $H_0 = 72\text{km s}^{-1}\text{ Mpc}^{-1}$, $\Omega_m = 0.27$, and $\Omega_\Lambda = 0.73$ and $\Omega_k = 0$. Each of the `Yggdrasil` and `LYCAN` models were redshifted from $z - 0.1 - 15$ with $\Delta z = 0.1$ step sizes and the `FSPS` models were redshifted from $z = 0.1 - 5$ with $\Delta z = 0.01 - 0.3$ step sizes, depending on the SED. The synthetic AB magnitude m for each SED at each redshift in every CANUCS filter was then computed using F_ν by taking

$$m = -2.5\log_{10}(F_\nu) + C \quad (6)$$

where C is the zeropoint such that $m = C$ for an object with a certain F_ν. The zeropoints are specific to the photometric system used. In this case we use the AB magnitude system, which has a zeropoint defined by a flat SED with $f(\nu) = 3631$ Jy. Since the filter throughput curves are different for each filter, the zeropoints must be calculated for each filter. This is done through the same process as above, but this time using $f(\nu) = 3631$ Jy in Eq. 4 instead of $f(\nu)$ given by the SED. The resulting value of F_ν is then used to measure the zeropoint through $C = 2.5\log_{10}(F_\nu)$. A subset of the synthetic magnitudes were computed in this way, but in practice it is much simpler to use a python package to compute the magnitudes of the hundreds of SEDs used in this work. Thus, we use the python package `synphot` to compute the synthetic magnitudes for all the SEDs, after confirming that those results agree with the computations described above.

Once the synthetic magnitudes were computed for each of the SEDs at various redshifts, several different colour vs. redshift diagrams were created. An example is shown in Figure 3.4 which shows four colours of a `Yggdrasil` SED over $3.5 < z < 6$. These diagrams were used to search for colour excesses that were driven by strong emission lines, specifically the Hα and [OIII] + Hβ lines. The examples in Figure 3.4 summarize the main results of this process: EELGs produce clear signatures in medium-band imaging by driving extreme colours in filters containing the Hα and [OIII] + Hβ lines. They commonly have colours of > 1 magnitude, even reaching colours of ~ 2 magnitudes in some cases. This is in contrast to other galaxy populations which have much less extreme colours, usually < 0.5 mag. The extreme colours of EELGs combined with the mild colours of other galaxies make EELGs relatively easy to identify in imaging data. This is especially true when searching for EELGs with *both* extreme Hα and [OIII] + Hβ emission, since this creates a unique pattern that is not easily replicated by other galaxy populations. These diagrams were used to define an initial set of colour selections that can target EELGs using medium-band flux excesses over $1.7 \lesssim z \lesssim 6.7$. These colour cuts were then tested and modified by estimating the completeness and contamination of each colour cut, discussed below.

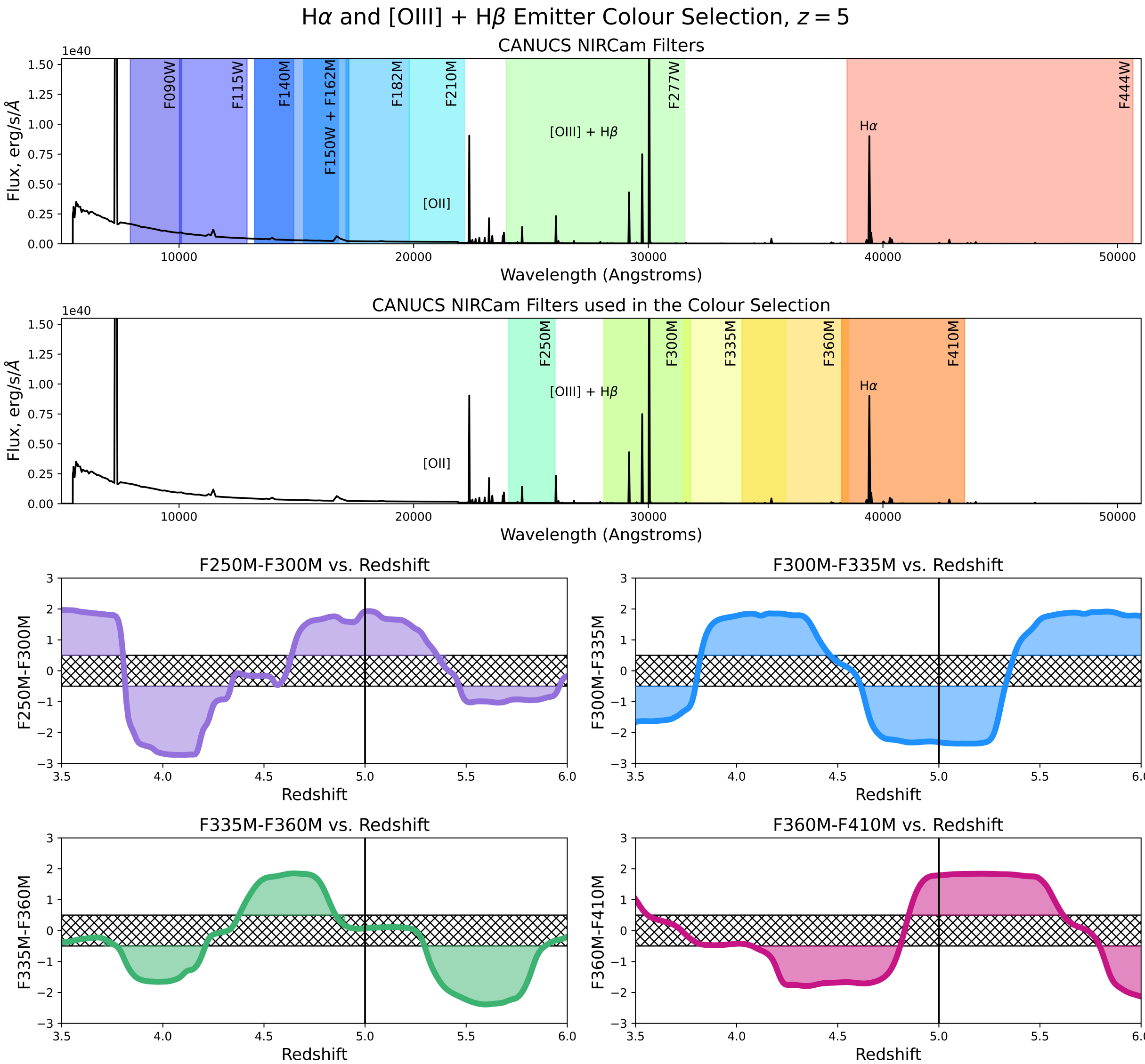

Figure 3.4: An example demonstrating the extreme colours EELGs create in neighbouring medium-band filters. The top two panels show a `Yggdrasil` SED overlaid on filter the coverage for the filters used in the example colour selection (second panel, F250M, F300M, F335M, F360M, and F410M) and the rest of the filters used in the CANUCS NIRCam flanking fields (first panel, F090W, F115W, F140M, F150W, F162M, F182M, F210M, F277W, and F444W). The bottom four panels show how four colours evolve with galaxy redshift, which are used to select EELGs over $3.5 \lesssim z \lesssim 5.5$. The hatched regions indicate colours of ± 0.5, demonstrating how the Hα and [OIII] + Hβ emission lines drive strong colour excesses in the medium-bands. An animated version of this figure is available online here: https://www.youtube.com/watch?v=bTjjjyFRJys

3.4 Completeness & Contamination

Completeness and contamination of the colour selections was assessed by modifying the synthetic observations described in §3.3 to include photometric scatter. This was done by defining a Gaussian distribution corresponding to a certain signal-to-noise (S/N) ratio, then adding scatter to the synthetic observations by drawing 1000 random data points from that distribution. These were then added to the synthetic flux observed for a given SED/filter combination, creating 1000 different "versions" of each SED at a given S/N. Not all SEDs had photometric scatter added to them, as there were far too many SEDs used to create synthetic observations. Instead, a subset of SEDs were chosen that were the most representative of the galaxy population and the photometric scatter was added to those synthetic observations. Various values of S/N were used in this process, ranging from S/N $= 1$ to S/N $= 30$.

Once various amounts of photometric scatter had been added to the set of synthetic observations, completeness fractions were calculated for the colour selections. This was done by applying a given colour cut to each of set of synthetic observations with photometric scatter. The completeness fractions are then simply the number of galaxies selected when photometric scatter is added to the data vs. how many are selected in the idealized scenario where there is no photometric scatter. This process was repeated for a variety of different colour cuts, e.g. using a 0.5 mag colour vs. a 0.3 mag colour. The results of this process are summarized in Figure 3.5, which shows the completeness fractions for a set of colour cuts as a function of S/N averaged over filters with continuum emission, for emission lines of varying EW. This plot shows that the colour selections work the best for the highest S/N galaxies which have the largest EWs. These most extreme cases (right panels) can have completeness fractions of $> 80\%$, sometimes even reaching $\sim 100\%$ completeness. The completeness fractions can be significantly worse for less extreme systems (left panels), which have generally much lower completeness fractions, sometimes even 0% at all S/N (in which case the completeness curves are not plotted).

Calculating contamination fractions is much more challenging than completeness fractions since it requires estimates on the abundances of EELGs vs. contaminants. As such, we do not calculate

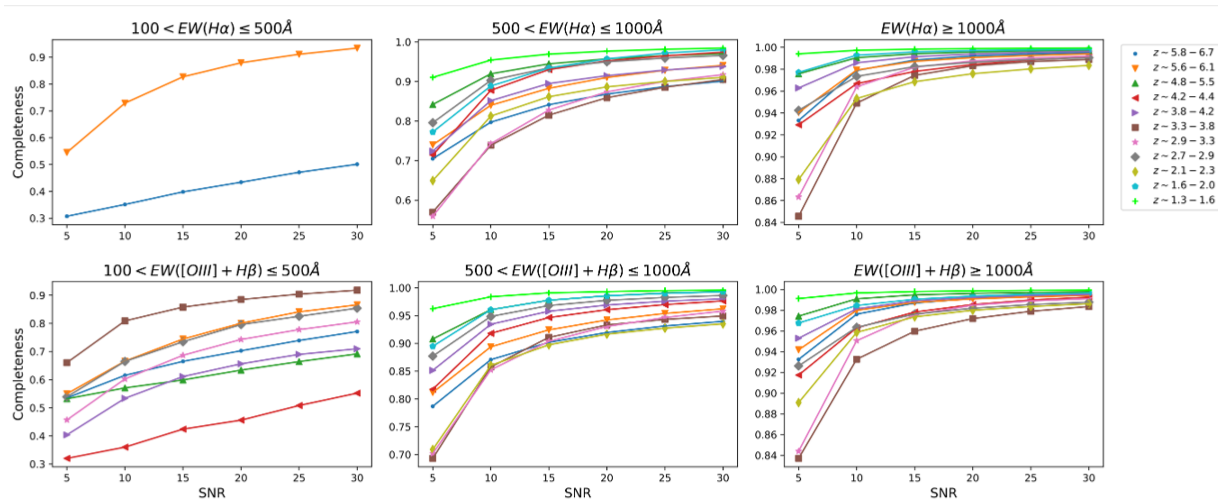

Figure 3.5: Examples of completeness fractions of various colour cuts. Each plot shows the completeness fraction as a function of S/N for the Hα (top) and [OIII] + Hβ (bottom) lines of various EWs (different rows). The curves are not plotted for colour selections that have 0% completeness for all S/N values. This is most relevant for the two panels on the left, which have many selections with 0% completeness fractions and thus fewer curves plotted than the middle and right panels.

the contamination fractions themselves, and instead assess the sample contamination in a *relative* sense. The amount of contamination was measured in a similar way as the completeness fractions were, but this time by simply looking at the number of other galaxies selected for various colour cuts at various S/N. The effect of different colour cuts on contamination was then assessed by looking at the number of galaxies one set of colour cuts selected vs. another when applied to the same parent sample of simulated galaxies, instead of using fractions as was done with the completeness fractions.

Interestingly, the main contaminants for these colour cuts came from higher-redshift [OII] and [OIII] + Hβ emitters, since the wavelength separation between [OII] and [OIII] + Hβ lines is similar to the separation between [OIII] + Hβ and Hα. In this case, flux excesses driven by [OII] emission were mistaken for emission from [OIII] + Hβ and emission from [OIII] + Hβ was mistaken for emission from Hα. A similar effect can be observed for very low-redshift star-forming galaxies, which can have strong IR emission lines that mimic the signatures of [OIII] + Hβ and Hα emitters.

The overall results of these tests is that the colour selections are more complete and have the least amount of contamination for high S/N objects and for galaxies with the highest EWs. A final set of colour selections was then defined by picking the selections that maximized completeness but minimized contamination, while also being realistic regarding the S/N and EWs that would be seen in the galaxy population. The completeness fractions of the colour selections range from $\sim$70% - 100%, depending on the selection criteria, S/N, and strength of the emission line.

It is important to reiterate that while it is possible (and quite common) to select EELGs based on a single emission line complex, we choose to select EELGs based on two emission line complexes ([OIII] + Hβ and Hα). The results of the contamination tests highlight why we made this decision: the colour selections have higher completeness and lower contamination when targeting two emission line complexes, since it is much more challenging mimic the signature created by two spectral features than it is to mimic the signature created by one spectral feature. Selecting on two emission lines is thus able to break redshift degeneracies that would appear when selecting based on one emission line.

3.5 Colour Selections

With the results of the completeness and contamination analysis described above, we define a set of ten colour cuts that select EELGs over $1.7 \lesssim z \lesssim 6.7$. These colour selections are presented in Table 3, which includes information about the redshifts the selections target (Col. 2) and the colour cuts (Col. 1). As discussed above, these colour selections target galaxies with *two* strong emission lines: [OIII] + Hβ and Hα emission. Thus, the colour cuts each select galaxies based on at least two strong colours, one that targets Hα emission and one that targets [OIII] + Hβ emission. There are certain selection criteria that select galaxies based on three colours. This is done to take advantage of the overlap between some of the medium-bands, particularly the overlap between F335M and F360M which can provide more robust selections than simply using two colours. The tests described above show that our colour selections can effectively identify galaxies with EW(Hα) $\gtrsim$ 500 Å and EW([OIII] + Hβ) $\gtrsim$ 1000 Å at all redshifts targeted in this work.

Additionally, as discussed in §1.4 medium-band colour cuts are able to select EELGs based on line flux without the need for strong continuum emission. This provides a powerful way to search for faint emission line only sources which are challenging to identify using other techniques. However, targeting very faint galaxies comes with its own challenges including increased contamination. Thus, as a first work on using NIRCam medium-bands to identify EELGs with colour selections, we decide to keep the process simple and employ a S/N cut in our selection criteria. Specifically, we require S/N ≥ 4 in filters with Hα and [OIII] + Hβ emission lines and S/N ≥ 2 on average in the underlying continuum. Doing so allows us to obtain a robust sample of EELGs with high completeness fractions.

3.6 Summary

In this section, we described the colour selections used to select the galaxies in our sample. The colour selections were defined based off of models of high-redshift EELGs, which are representative of the EELG population at many redshifts. These are discussed in §3.1, and include two sets of SEDs which were generated from the `Yggdrasil` SPS code: one set of "toy models" of EELGs (the `Yggdrasil` models) and one set of SEDs modelled after $z \approx 7$ galaxies from four cosmological simulations (the `LYCAN` models). Examples of these models are shown in Figure 3.1. In §3.2 we discussed the SEDs used to model other galaxy populations which could contaminate our sample of EELGs. This was done by generating SEDs of a variety of galaxies using the `FSPS` code, with examples of these SEDs in Figure 3.3.

We then discussed creating synthetic observations of these SEDs in the CANUCS NIRCam filters in §3.3, which were used to create a set of colour cuts capable of selecting EELGs. These initial set of colour cuts were then modified by assessing the completeness and contamination of the colour cuts by adding photometric scatter to the synthetic observations, as discussed in §3.4. Finally, §3.5 discusses the final set of colour selections defined through this process, which are presented in Table 3.

Colour Cut Col. 1	Redshifts Selected Col. 2	Emission-Line Filters Col. 3	Continuum Filters Col. 4
$F410M - F444W > 0.5$ $F360M - F410M < -1$	$z = 5.8 - 6.7$	Hα: F444W [OIII] + Hβ: F360M	F140M, F162M, F182M, F210M F410M
$F410M - F444W > 0.5$ $F335M - F360M < -1$	$z = 5.6 - 6.1$	Hα: F444W [OIII] + Hβ: F335M	F140M, F162M, F182M, F210M F410M
$F360M - F410M > 0.5$ $F335M - F360M < -1$	$z = 5.3 - 5.7$	Hα: F410M [OIII] + Hβ: F335M	F140M, F162M, F182M, F210M F360M
$F360M - F410M > 0.5$ $F300M - F335M < -1$	$z = 4.8 - 5.5$	Hα: F410M [OIII] + Hβ: F300M	F115W, F162M, F182M, F360M
$F300M - F335M > 0.5$ $F360M - F410M < -0.5$ $F250M - F300M < -1$	$z = 4.2 - 4.4$	Hα: F335M [OIII] + Hβ: F250M	F115W, F140M, F162M, F410M
$F300M - F335M > 0.5$ $F335M - F360M < -0.5$ $F250M - F300M < -1$	$z = 3.8 - 4.2$	Hα: F335M [OIII] + Hβ: F250M	F115W, F140M, F162M, F300M F410M
$F250M - F300M > 0.5$ $F210M - F250M < -1$	$z = 3.3 - 3.8$	Hα: F300M [OIII] + Hβ: F210M	F090W, F115W, F140M, F250M F360M
$F210M - F250M > 0.5$ $F182M - F210M < -1$	$z = 2.7 - 2.9$	Hα: F250M [OIII] + Hβ: F182M	F090W, F115W, F300M, F335M
$F182M - F210M > 0.5$ $F162M - F182M < -1$	$z = 2.1 - 2.3$	Hα: F210M [OIII] + Hβ: F162M	F090W, F182M, F250M
$F162M - F182M > 0.5$ $F140M - F162M < -1$	$z = 1.7 - 2$	Hα: F182M [OIII] + Hβ: F140M	F090W, F162M, F210M, F250M

Table 3: List of colour selections used in this work. The table includes the colour cuts (Col. 1), the redshifts they probe (Col. 2), filters containing the Hα and [OIII] + Hβ emission lines (Col. 3), and the filters used to estimate the continuum emission (Col. 4). Each set of colour cuts has at least two criteria, one that targets extreme [OIII] + Hβ emission and one that targets extreme Hα emission.

4 Analysis

4.1 Initial Sample

Based on the colour and S/N cuts described in §3, we select 118 objects over $1.7 \lesssim z \lesssim 6.7$ which have *both* strong Hα (EW(Hα) $\gtrsim 500$ Å) and [OIII] + Hβ (EW([OIII] + Hβ) $\gtrsim 1000$ Å) emission. The sample of 118 objects was selected out of 7729 objects in the catalogue with usable photometry, and 4306 objects which pass the S/N cuts. While the colour selections give an estimate of galaxy redshift based on what filters the Hα and [OIII] + Hβ must be in to drive the observed colour excesses (see Table 3), more precise redshifts are required for the analysis. These were obtained by determining the photometric redshifts of each galaxy using the code `EAZY` (Brammer et al. 2008). `EAZY` was run using a set of 16 templates from from `FSPS` (Conroy et al. 2009, Conroy & Gunn 2010) and Larson et al. (2022), and by limiting the allowed best-fit redshifts to the redshift ranges implied by the colour selections. This allowed us to obtain a precise redshift for each galaxy that is consistent with the findings of the colour selections. Running `EAZY` over a wider range of redshifts ($0.01 < z < 20$, as commonly-used when running `EAZY`) yields results that are mostly consistent with limiting the allowed redshifts to those implied by the colour selections. However, there are a small number of objects whose best-fit redshift from `EAZY` disagrees with the colour selections, with `EAZY` typically finding a very low-redshift solution. Thus, it is necessary to limit the allowed redshifts as described above. The photometric redshifts for the galaxies in this sample are shown in Figure 4.1, which shows the redshift coverage of the colour selections is "patchy". This is a result of using strong emission lines to select galaxies, since that restricts the selected redshifts to places where the strong flux excesses can be observed. Overall, the colour selections provides good redshift coverage over the entire $1.7 \lesssim z \lesssim 6.7$ range.

Figure 4.2 shows three examples of the galaxies in this sample. All three examples show flux excesses in two filters driven by strong [OIII] + Hβ and Hα emission, and two of the examples (ID 1203427 and 1202967) exhibit blue continuum slopes and show clear evidence of a Lyman break. However the third example (ID1205006) has a very red continuum (due to large amounts of dust, see §4.3) resulting in the absence of a Lyman break. This example highlights the ability of medium-band colour selections to select galaxies based on emission line EW, with no dependence on strong rest frame UV-optical continuum. Objects such as these are similar to CEERS-93316 (Arrabal Haro et al. 2023), which have been shown to contaminate samples of photometrically selected very high-redshift galaxies (see also Zavala et al. 2023, as discussed in §1), and which have been found at high-redshifts (Endsley et al. 2023a). Thus, this example shows that medium-band

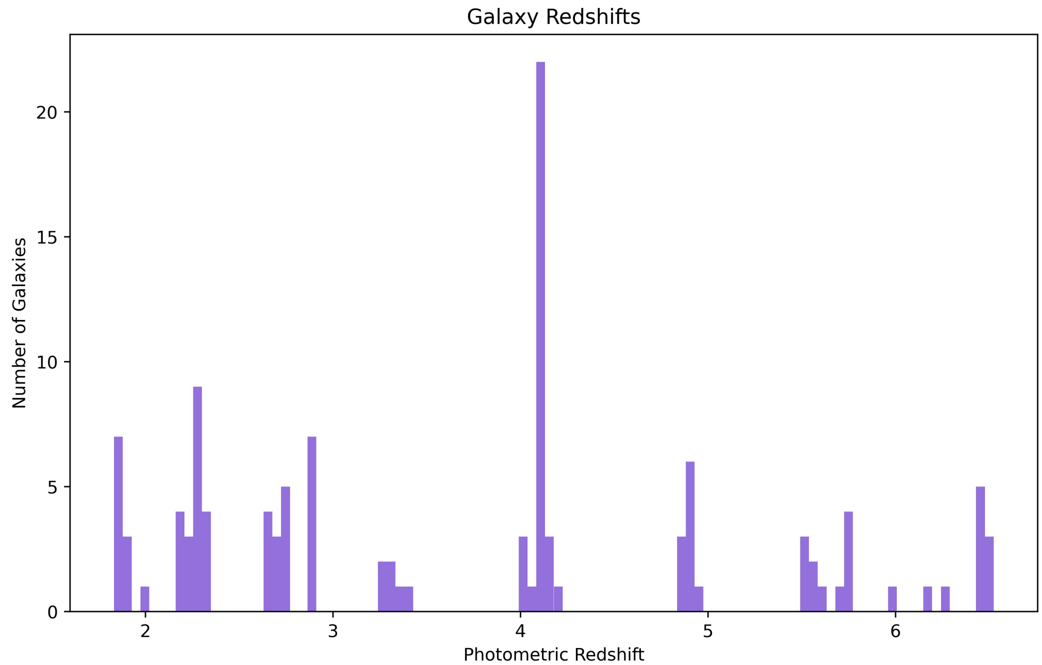

Figure 4.1: Histogram showing the EAZY photometric redshifts of the 118 galaxies in this sample. The colour selections select galaxies over $1.7 \lesssim z \lesssim 6.7$ in a "patchy" way. This is a reflection of how the colour selections target flux excesses in the medium-bands which will only occur at specific redshifts.

colour cuts can provide a useful tool in the search for very high-redshift galaxies by identifying lower-redshift interlopers in those samples. Additionally, the lack of continuum emission in the bluer filters of ID1205006 (such as F115W and F150W) suggests that these colour selections will be able to select very low mass galaxies for which no continuum emission can be detected in all or most of the filters. As discussed in §1, the faintness of the continuum emission in these "emission line only" galaxies makes them challenging to detect using conventional methods, meaning the medium-band filters provide a unique and powerful way to search for this population of galaxies.

4.2 Rest Frame Equivalent Widths

The rest frame EW([OIII] + Hβ) and EW(Hα) were calculated directly from the photometry for all the galaxies in the sample. The definition of EW is shown in Eq. 1, which turns into Eq. 7 when

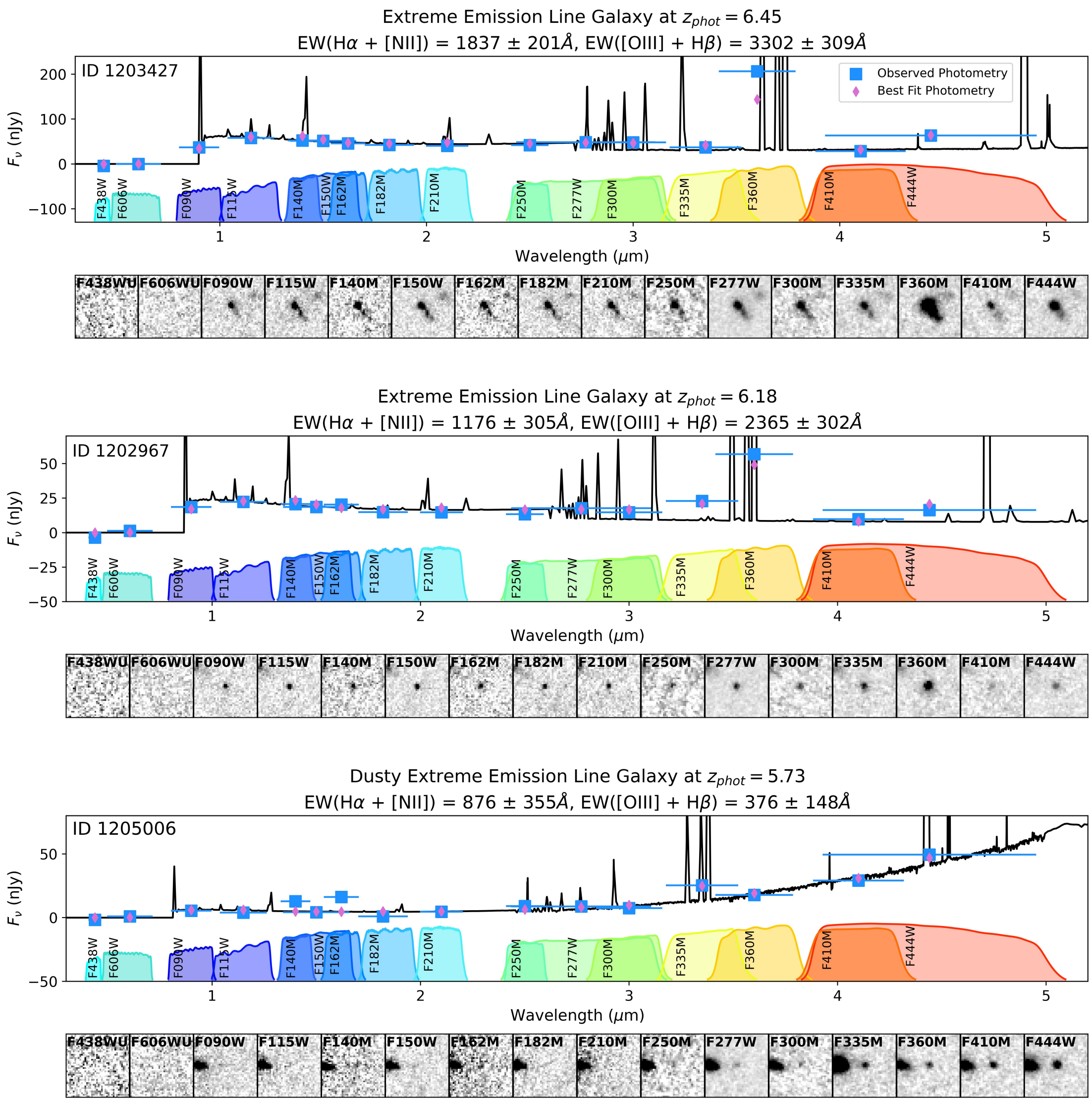

Figure 4.2: Examples of three EELGs identified in this work. Each example has $3'' \times 3''$ cutouts of the galaxy in the fourteen NIRCam filters and two WFC3/UVIS filters used in this work (bottom panels), as well as the filter throughput curves, photometry (blue squares), the best-fit SED from `EAZY` (black curves), and the predicted photometry from `EAZY` (purple diamonds). The first two SEDs (ID 1203427 and 1204847) have blue continuum fluxes and strong Lyman breaks, however the third example (ID 1205006) has a very red continuum and no visible Lyman break. This example demonstrates the ability of the medium-bands to select EELGs without the need for strong continuum emission, which can select faint galaxies and identify objects such as CEERS-93316 (Arrabal Haro et al. 2023). The best-fit SEDs (black curves) and predicted photometry (purple diamonds) in this figure are from photometric redshift code `EAZY` (Brammer et al. 2008), using the set of templates outlined in Larson et al. 2022. The best-fit SEDs were generated by forcing `EAZY` to fit the photometry at the redshift implied by the colour selections.

calculating EWs directly from the photometry.

$$\mathrm{EW}_{\text{Rest Frame}} = \frac{f_{\text{observed}} - f_{\text{continuum}}}{f_{\text{continuum}}} \times \frac{\text{Filter Bandwidth}}{1 + z_{\text{EAZY}}} \tag{7}$$

where f_{observed} is the flux density of the filter containing the relevant emission line (listed in Table 3 column 3), $f_{\text{continuum}}$ is the continuum flux in the filter containing the emission line, the Filter Bandwidth is the bandwidth of the filter (yet again) containing the emission line (listed in Table 1 column 4) and z_{EAZY} is the best-fit redshift from `EAZY`. The $(1+z_{\text{EAZY}})^{-1}$ term in Eq. 7 is necessary to convert the observed frame EW to rest frame EW, since redshifting the SED increases the EW in the observed frame. The f_{observed} is simply obtained directly from the photometric catalogue, while $f_{\text{continuum}}$ was estimated from the photometry by using multiple filters that sample the continuum emission. In this work, we use the photometry from the $0.7''$ apertures which sums up the total counts observed in a circular aperture of $0.7''$ diameter around the object using images convolved to the F444W point spread function. The $f_{\text{continuum}}$ was measured by approximating the continuum flux of the galaxy with a power law, $f_\nu \propto \lambda^\alpha$ and using that fit to estimate the underlying continuum flux in the relevant filter. This power law fitting can be done in linear space, however, in practice it is much more straightforward to carry out this calculation in log-log space in which case the power law fit turns into a straight line fit (i.e. fit $\log(f_\nu)$ vs. $\log(\lambda)$ with a straight line instead of fitting f_ν vs. λ with a power law). Thus, for the sake of simplicity we convert the observed photometry into log-log, fit that with a straight line and compute $\log(f_{\text{continuum}})$, then convert $\log(f_{\text{continuum}})$ into $f_{\text{continuum}}$ to be used in Eq. 7.

An example of this continuum fitting is shown in Fig. 4.3, which shows the continuum fitting for the first example in Fig. 4.2 (ID 1203427). The grey shaded regions highlight the filters used to estimate the continuum emission, while the pink shaded region is the filter containing the [OIII] + Hβ complex and the purple region is the filter containing the Hα emission line. Not all filters were used to estimate the continuum emission since not all filters are representative of the continuum emission. For example, in Figure 4.3, the Lyman break can be observed in the bluest filters (at $\sim 0.5 - 1\mu$m), while contamination from the [OII] and Balmer emission lines can be seen in filters

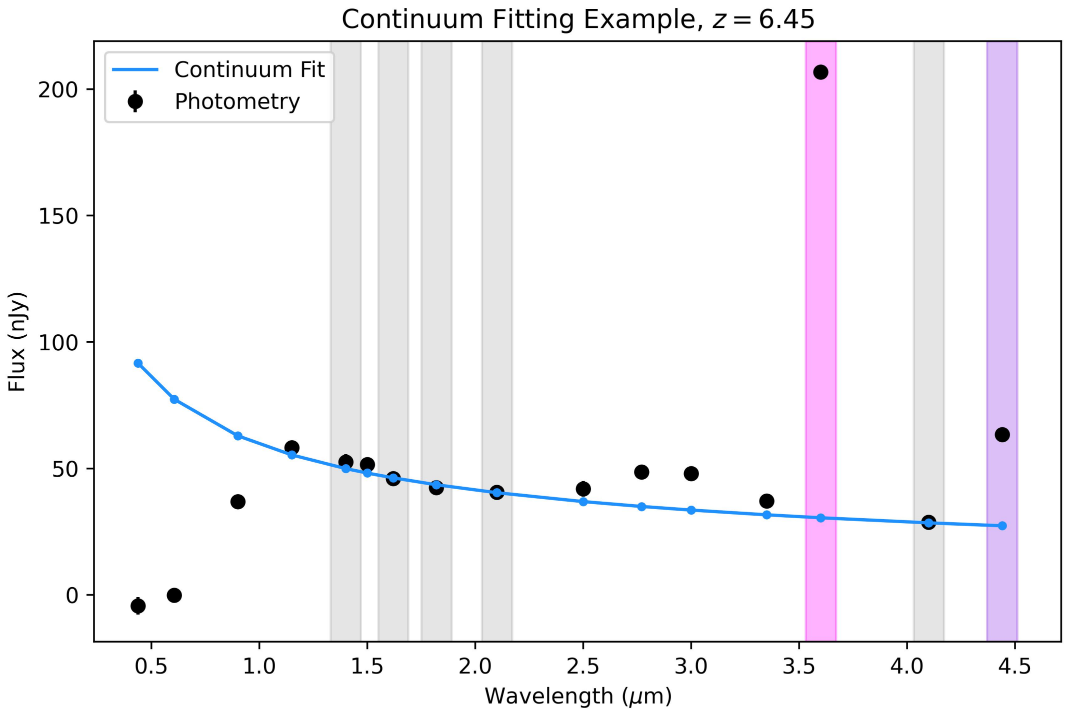

Figure 4.3: An example of the continuum fitting process required to measure EWs from the medium-band filters. The observed data points are the black circles, the filters used in continuum fitting are shown in the black shaded regions (Table 3 Col. 4), and the pink and purple shaded regions are the filters used to measure the flux excesses of [OIII] + Hβ and Hα, respectively (Table 3 Col. 3). The continuum fit is then shown in blue.

at $\sim 2.5-3\mu$m. Thus, it is necessary to exclude these "contaminated" filters from the continuum fitting. Which filters are contaminated with what spectral features will change as a function of redshift, so a different set of filters were chosen to estimate the continuum fluxes for each of the colour cuts, which are shown in Table 3. The continuum filters were chosen to avoid using filters that may be contaminated with other emission lines (such as the [OII], Balmer, or Paschen lines) at the galaxy redshift. Errors and uncertainties in measuring the EWs in this way will be discussed in detail in §5.3.2.

Figure 4.4 shows the distribution of EW([OIII] + Hβ) and EW(Hα) for the entire sample (top panel), and with the sample separated into four redshift bins (bottom panels). These redshift bins were chosen arbitrarily and highlight the way that EW distributions change with redshift. This figure demonstrates that very high EW systems do exist over $1.7 \lesssim z \lesssim 6.7$, with EW > 1000Å in both [OIII] + Hβ and Hα, sometimes even reaching EW ~ 3000Å. Other searches for EELGs have revealed similarly high EW objects (e.g. Smit et al. 2015, Robertson et al. 2015, Endsley et al. 2021, Stefanon et al. 2022, Rinaldi et al. 2023 at high-redshift $z \gtrsim 5$, and Reddy et al. 2018, Boyett et al. 2022, Onodera et al. 2020 at intermediate-redshift, $z \lesssim 5$), however, the most extreme objects are quite rare and represent only a small sample of the total star-forming galaxies at any given redshift.

4.3 Physical Properties

The physical properties (stellar masses, specific star formation rate, metallicity and dust attenuation) of the EELGs were determined using the `Dense Basis` (Iyer et al. 2019) SED fitting code. Fitting was performed by the CANUCS team using the Kron apertures (Kron 1980), which is an aperture designed to fully encapsulate all of an object's flux. This is a larger aperture than the $0.7''$ apertures used in §4.2, which is necessary to accurately measure physical properties such as stellar masses. In order to perform the SED fits, we assume the Calzetti (2001) dust law, Kroupa (2001) IMF, and at the best-fit redshift from `EAZY` (see §4.1). Additionally, `Dense Basis` was allowed stellar masses of $7 < \log(M_\star/M_\odot) < 12$, dust attenuation of $0 < A_V < 4$, and metallicities of $-2 < \log(Z/Z_\odot) < 0.3$, (using flat priors for all properties). The results of the `Dense Basis` fitting are shown in Figure 4.5, and show that our sample of galaxies has properties that are consistent with typical EELGs at both high-redshift (e.g. Sun et al. 2022, Asada et al. 2022) and intermediate-redshift (e.g. Tang et al. 2019). The galaxies in our sample are typically low mass (median $\log(M_\star/M_\odot) = 8.02$), low metallicity (median $Z = 0.14Z_\odot$), with little dust attenuation (median $A_V = 0.18$ mag), and high specific star formation rates (SSFR, median $SSFR = 1.18 \times 10^{-8}/yr$, or a median SFR of SFR=). For reference, typical properties of star-forming galaxies at these redshifts are: $\log(SFR) \sim -1-2$ at $z \sim 2.7-6$ for galaxies with $\log(M/M_\odot) \sim 8.5-11$ (e.g. Speagle et al. (2014), Shapley et al. (2023)), stellar masses of $\log(M/M_\odot) \sim 9.11$ over $z \sim 2.7-6$ (e.g. Shapley et al. (2023)), metallicities of $Z = 0.4Z_\odot$ (e.g. Reddy et al. (2022)), and dust attenuation of $A_V \sim 0.2$ (e.g. Shapley et al. (2023)).

Furthermore, a visual inspection of the images reveals most of the EELGs are compact with

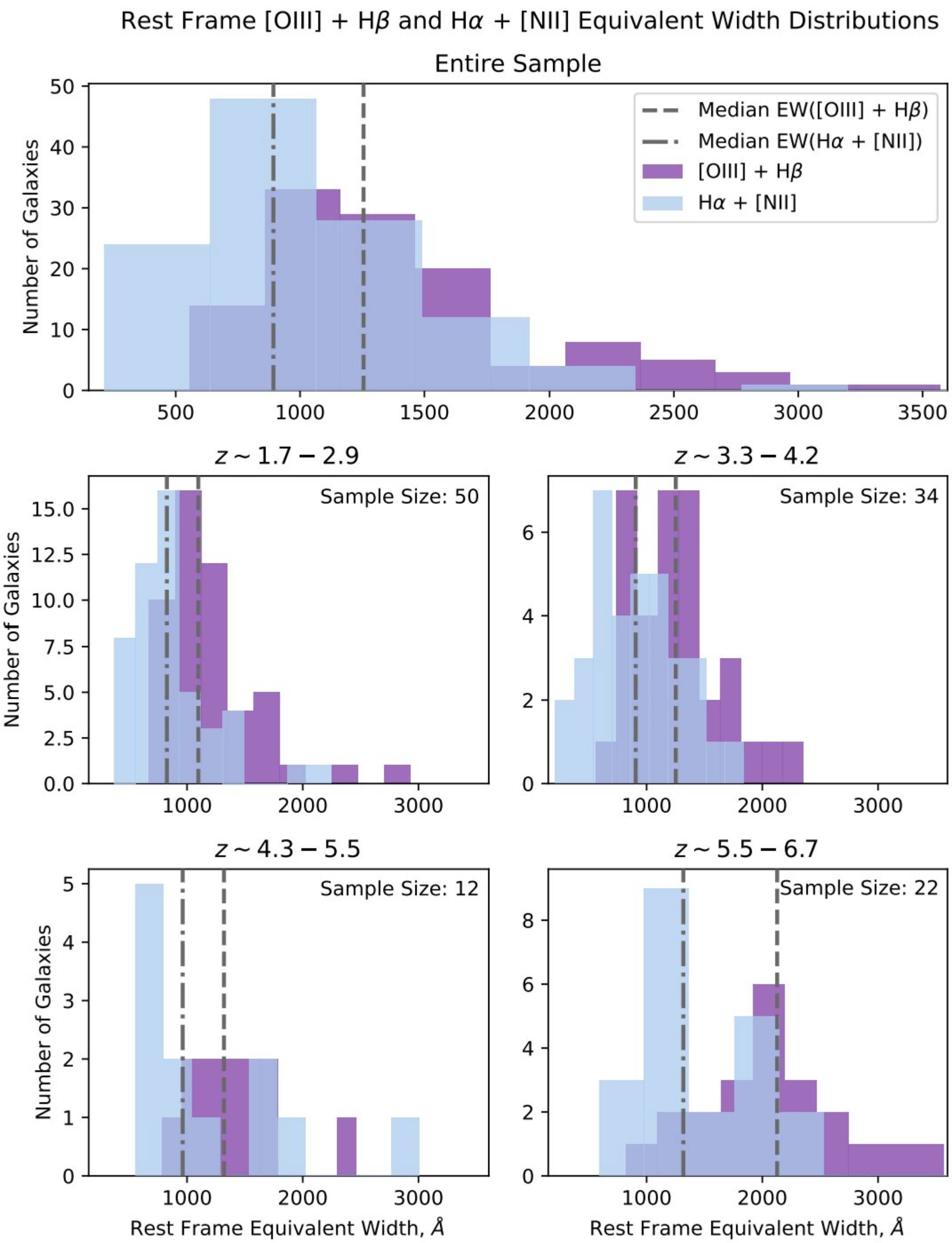

Figure 4.4: Histograms showing EW([OIII] + Hβ) (purple) and EW(Hα) (blue) for the entire sample (top panel) and as a function of redshift (bottom four panels). Each panel also shows the median EW([OIII] + Hβ) (gray dashed line) and median EW(Hα) (gray dash dotted line).

little to no structure, which is typical of EELGs. However, $\sim 20\%$ of our sample show evidence of interactions or mergers, such as example 1 in Figure 4.2 (ID 1203427). While it is interesting to note the merger/interaction rate of galaxies in our sample, it is important to highlight that there is a large uncertainty on this number since it is based on a visual inspection of the images and does not involve quantitative morphological criteria to identify merging/interacting galaxies.

Additionally, Figure 4.6 shows the variation of stellar mass with redshift (left), specific star formation rate with redshift (middle), and star formation rate (SFR) with stellar mass (left). These plots highlight several features of the galaxy sample. First, the left panel shows that the stellar masses increase with redshift. This is a selection effect created by the use of S/N cuts in the colour selections. While these cuts ensure the quality of EELGs selected by the colour cuts, it also requires higher-redshift galaxies to be brighter and thus more massive than lower-redshift galaxies in order to meet the S/N criteria and be selected. This behaviour is why the median values in four redshift bins reported in Figure 4.7 (discussed in §4.4), is restricted to galaxies with stellar masses of $7.9 < \log(M_\star/M_\odot) < 8.5$, which is a mass range that is covered in all four bins.

Additionally, the middle (SSFR vs. redshift) and right (SFR vs. stellar mass) panels show that our sample of galaxies follow two well known trends of star-forming galaxies. The first is shown in the middle panel which demonstrates that galaxies in our sample exhibit generally higher SSFRs at earlier times. This is a feature that has been observed in other samples of star-forming galaxies over various redshift ranges (e.g. Reddy et al. 2018). Secondly, the right panel demonstrates that galaxies in this sample follow the stellar mass-SFR relation for star-forming galaxies. This "star-forming main sequence" is the trend where galaxy SFR increases with increasing mass. This has been observed over a wide range of redshifts (e.g. Speagle et al. 2014, Popesso et al. 2022 over $z \sim 0-6$), with the right panel of Figure 4.6 confirming that our sample follows this trend over $z \sim 1.7-6.7$.

4.4 Dependence of EWs on Physical Properties and Redshift

Figure 4.7 shows the dependence of the rest frame [OIII] + Hβ and Hα EWs with stellar mass (left) and redshift (right), including the median values for galaxies with $7.9 < \log(M_\star/M_\odot) < 8.5$ (a mass

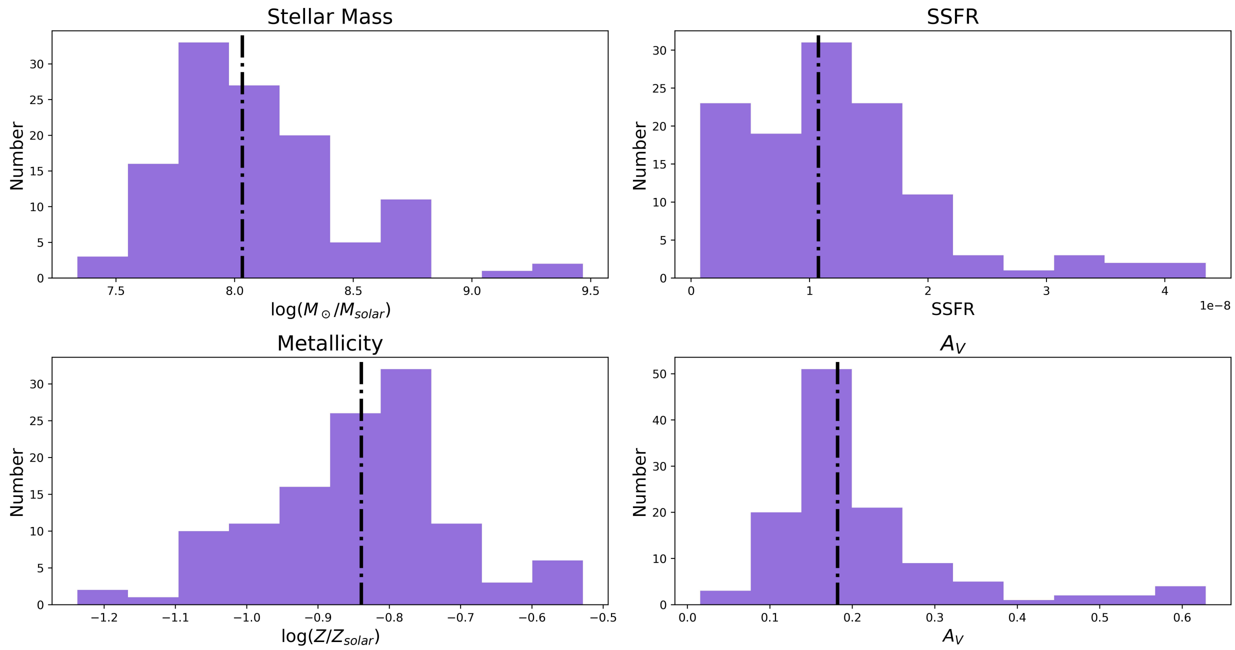

Figure 4.5: Histograms of the physical properties of galaxies in our sample as measured through the `Dense Basis` SED fitting. The galaxies in our sample have properties that are typical of EELGs: low stellar masses (median $\log(M_\star/M_\odot) = 8.02$, top left), high SSFR (median $SSFR = 1.18 \times 10^{-8}/yr$, top right), low metallicities (median $Z = 0.14Z_\odot$, bottom left) and little dust (median $A_V = 0.18$ mag, bottom right).

range that is covered in each of the redshift bins used in Figure 4.4). The left and right panels of Figure 4.7 illustrate several important points about our sample of EELGs. First, a visual inspection of the left panel of Figure 4.7 shows that our sample reproduces the known anti-correlation between rest frame EW(Hα) and stellar mass (e.g. Matthee et al. 2022, Onodera et al. 2020, Rinaldi et al. 2023, Sun et al. 2022). However, there does not appear to be any correlation between rest frame EW([OIII] + Hβ) and stellar mass. To test this, we performed the Spearman's rank-order correlation test on the distributions. The tests yield $t_{\mathrm{H}\alpha} = -0.18$, $p_{\mathrm{H}\alpha} = 0.045$, and $t_{[\mathrm{OIII}]+\mathrm{H}\beta} = -0.0033$, $p_{[\mathrm{OIII}]+\mathrm{H}\beta} = 0.97$, confirming that there exists an anti-correlation between EW(Hα) and stellar mass, and no correlation of EW([OIII] + Hβ) and stellar mass. Taken at face value, this trend of constant EW([OIII] + Hβ) with stellar mass indicates that metallicity of the EELGs may remain roughly constant with stellar mass. However, this conclusion is only tentative given that our sample contains selection biases for the strongest EWs, and therefore may be incomplete at lower EWs.

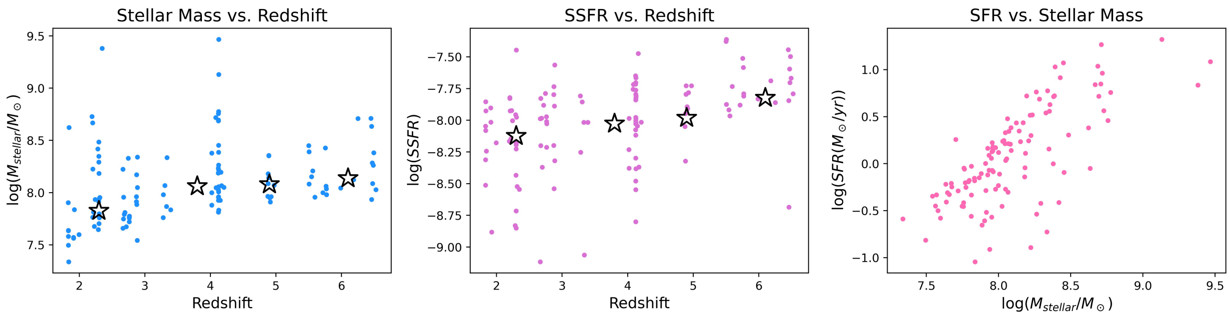

Figure 4.6: Left: Stellar mass vs. redshift. Middle: SSFR vs. redshift, right: SFR vs. stellar mass. The left and middle plots show the median values for galaxies in four redshift bins which are used in Figure 4.4 (black stars). Additionally, for the middle panel, these median values include only galaxies with $7.9 < \log(M_\star/M_\odot) < 8.5$, since this is a mass range covered in all four redshift bins (see left panel). The middle and right panels show that our sample of galaxies follow relations that have been previously observed with other galaxy samples, while the left hand plot highlights the selection bias of our sample.

Additionally, the right panel of Figure 4.7 shows evidence of increasing EW([OIII] + Hβ) and EW(Hα) with redshift, a trend which is also observed in Figure 4.4. The same behaviour has been observed in other populations of EELGs (e.g. Reddy et al. 2018, Matthee et al. 2022), and is generally attributed to higher SSFRs at earlier times (e.g. Reddy et al. 2018). While we do not establish a causal link between the evolution of EW and SSFR with redshift for galaxies in our sample, it is interesting to note that the SSFRs of galaxies in our sample do increase with redshift (middle panel of Figure 4.6).

4.5 Summary

The colour selections described in §3 were used to select a sample of 118 galaxies over $1.7 \lesssim z \lesssim 6.7$ (see Figure 4.1 for the distribution of redshifts selected) which have Hα (EW(Hα) $\gtrsim 500$ Å) and [OIII] + Hβ (EW([OIII] + Hβ) $\gtrsim 1000$ Å). Three examples of these galaxies are shown in Figure 4.2, which all show evidence of flux excesses in two filters from Hα and [OIII] + Hβ emission. The EW(Hα) and EW([OIII] + Hβ) for all galaxies in the sample were measured directly from the photometry by approximating the continuum emission with a power law, an example of which is shown in Figure 4.3. The distribution of EWs in our sample are shown in Figure 4.4, demonstrates

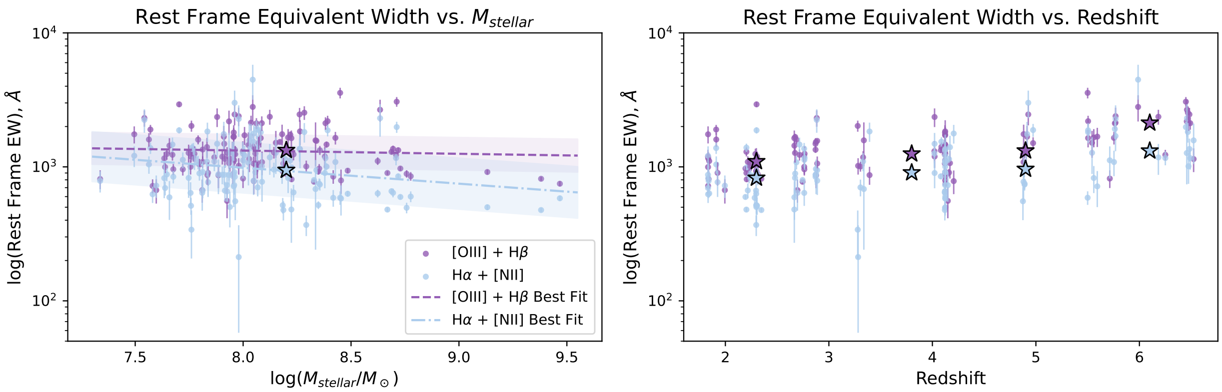

Figure 4.7: Left: EW([OIII] + Hβ) (purple) and EW(Hα) (blue) as a function of stellar mass, with a line of best-fit for EW([OIII] + Hβ) (dashed line) and EW(Hα) (dash dot line). The median EWs for galaxies with $7.9 < \log(M_\star/M_\odot) < 8.5$ are plotted as blue (Hα) and purple ([OIII] + Hβ) stars. Right: EW([OIII] + Hβ) (purple) and EW(Hα) (blue) as a function of redshift. Also plotted is the median EWs for galaxies in the same four redshift bins as Figure 4.4 with $7.9 < \log(M_\star/M_\odot) < 8.5$ as the blue (Hα) and purple ([OIII] + Hβ) stars.

that our sample contains some very high EW objects, sometimes reaching EW$\sim$ 3000Å.

SED fitting with the `Dense Basis` code shows that our sample of galaxies have properties that are consistent with EELGs: they are typically compact, low mass (median $\log(M_\star/M_\odot) = 8.02$), low metallicity (median $Z = 0.14Z_\odot$), with little dust attenuation (median $A_V = 0.18$ mag), and high SSFR (median $SSFR = 1.18 \times 10^{-8}/yr$), summarized in Figure 4.5. Additionally, galaxies in our sample have increasing SSFR with redshift and follow the "star-forming main sequence" (Figure 4.6). Finally, Figure 4.7 shows that EW(Hα) and EW([OIII] + Hβ) increase with redshift and EW(Hα) anti-correlates with stellar mass while EW([OIII] + Hβ) shows no correlation with stellar mass. Many of these trends have been observed in other populations of star-forming galaxies and EELGs.

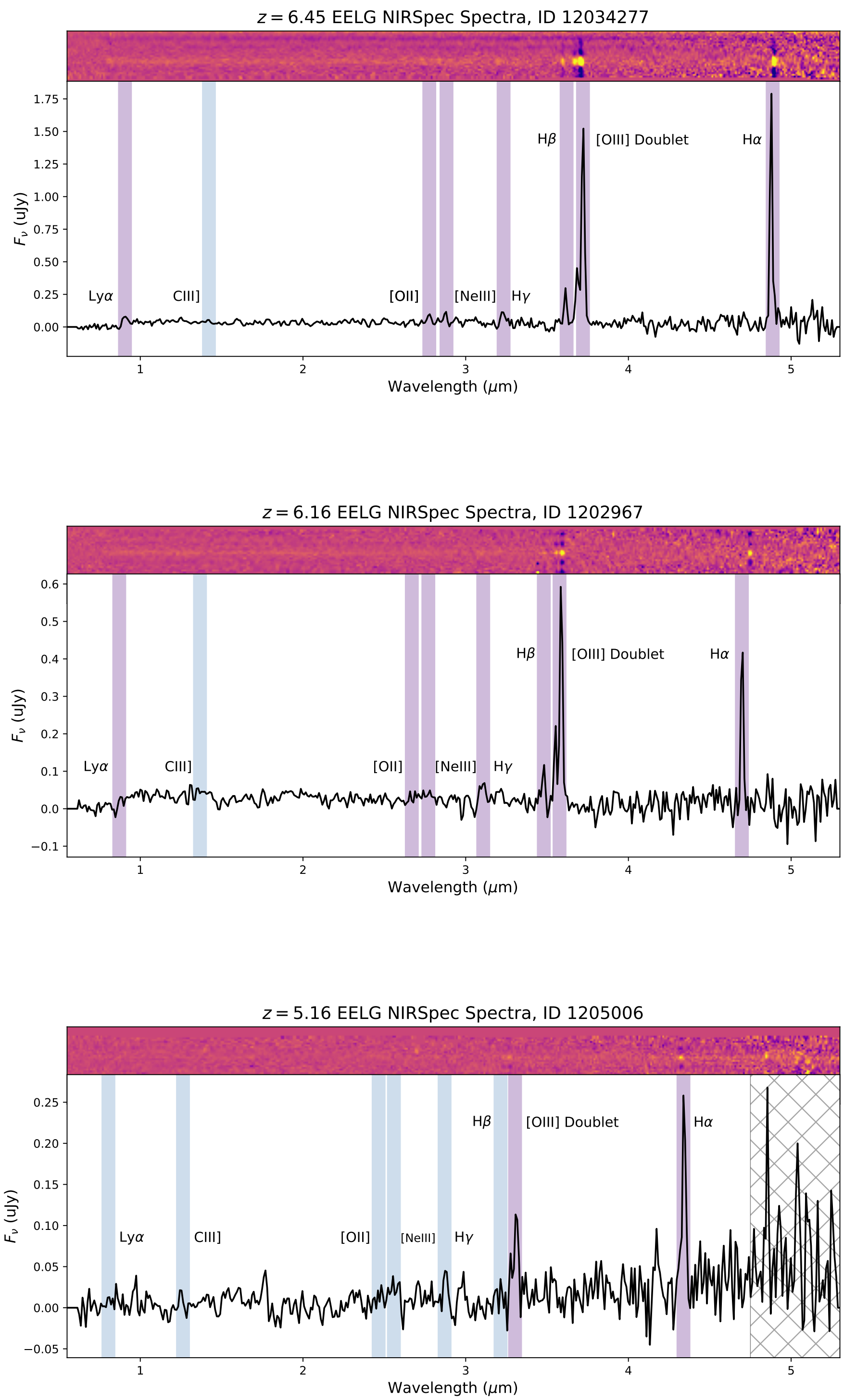

Figure 5.1: Examples of three NIRSpec spectra of EELGs in the sample. These correspond to the same examples shown in Figure 4.2

5 Effectiveness of Medium-Band Colour Selections & EWs

5.1 Low-Resolution Spectra

We obtained follow-up spectroscopy for 15 of the EELGs in our sample (see §4.1 for information on the sample and §2.2 for information on the spectroscopy), which is summarized in Table 4. Figure 5.1 shows three examples of these spectra, which correspond to the examples in Figure 4.2. In all cases the spectra confirm the nature of the EELGs, revealing that they each show strong Hα and [OIII] + Hβ emission. Many of the spectra also show evidence for other emission lines that were not targeted by the colour selections, including Lyα (only in ID12034277), [OII], and other Balmer lines. Thus, these spectra verify that medium-band colour selections are able to accurately select EELGs.

Included in the spectra is the very red galaxy (third example, ID1205006) which has no detectable Lyman break. As mentioned in §4.1, the very red continuum in this galaxy is driven by large quantities of dust, and galaxies such as these have been shown to contaminate samples of very high-redshift photometrically selected galaxies. The spectroscopic confirmation of the nature of this galaxy is particularly significant, since it verifies that medium-band colour selections are able to select galaxies without relying on continuum emission, and underscores the power of medium-band colour selections.

5.2 Spectroscopic Redshifts

Spectroscopic redshifts were obtained for all 15 of the NIRSpec spectra using an automated pipeline, and the photometric redshift vs. the spectroscopic redshift for the sample is shown in Figure 5.2 (recall that the photometric redshifts were determined by fitting the SEDs only at redshifts that agree with the colour selections). This plot shows an incredibly good agreement between the photometric and spectroscopic redshifts of these galaxies, with a mean absolute deviation of $\Delta z = 0.037$ between the spectroscopic and photometric redshifts (see also Table 4 Col. 2, 3). One of the objects (ID1205360) has a difference of $\Delta z = 0.64$ between the spectroscopic and photometric

ID Col. 1	z_{phot} Col. 2	z_{spec} Col. 3	EW(Hα) Photometry Col. 4	EW(Hα) Spectrum Col. 5	EW([OIII] + Hβ) Photometry Col. 6	EW([OIII] + Hβ) Spectrum Col. 7
1205360	1.83	1.89	824	725	1156	563
1203638	5.52	5.50	1870	1605	2186	2857
1203427	6.40	6.43	1973	1533	3073	3005
1202026	2.15	2.09	1391	1246	1830	2624
1202967	6.18	6.16	1171	-	2371	2220
1202540	4.90	4.94	735	754	1330	-
1204708	3.15	3.22	1994	1162	2210	2995
1202674	2.68	2.79	872	814	1486	151
1202544	3.31	3.32	702	711	1005	882
1200366	4.09	4.10	498	820	915	1557
1204983	2.28	2.27	596	627	971	881
1203207	2.73	2.77	880	-	865	833
1205780	4.09	4.13	1089	-	1404	-
1203539	5.04	5.09	3002	-	2462	-
1203111	2.87	2.86	964	925	1533	2058

Table 4: The redshifts and EWs measured from the spectra for each of the 15 objects with NIRSpec spectroscopy (ID numbers listed in Col. 1), along with the corresponding values measured from the photometry. The photometric redshifts are listed in Col. 2, the spectroscopic redshifts are listed Col. 3, the EW(Hα) measured from photometry/spectroscopy is listed in Col. 4/Col. 5, and the EW([OIII] + Hβ) measured from photometry/spectroscopy is listed in Col. 6/Col. 7. Objects that do not have EWs measured from spectroscopy are denoted by a '-' in place of the measurement, and all EWs are reported in Angstroms.

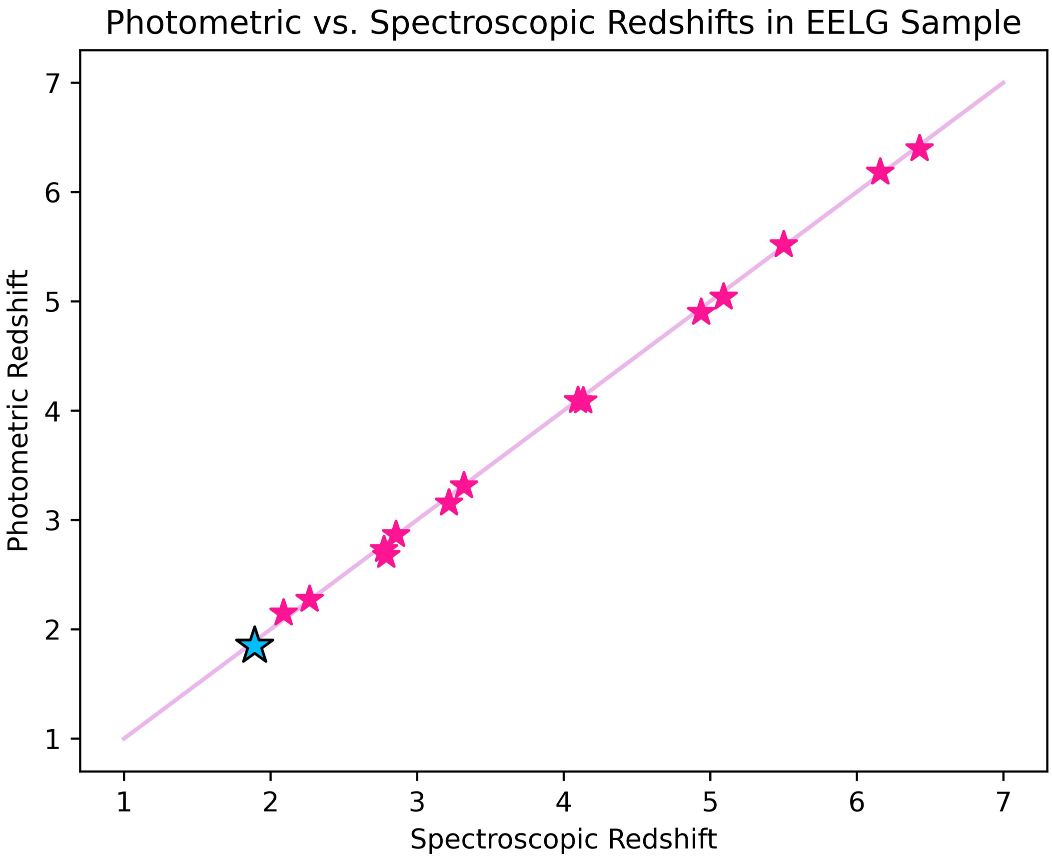

Figure 5.2: The photometric vs. spectroscopic redshifts for the EELGs with NIRSpec spectra. The spectroscopic and photometric redshifts agree with each other very well, with a mean absolute deviation of $\Delta z = 0.037$. The pink data points are spectroscopic redshifts measured from the automated spectra extraction software. The spectroscopic redshift in of the blue data point (with the black outline) measured this way is incorrect, thus we plot the spectroscopic redshift based on a visual inspection of the 1D spectra.

redshifts, with a $z_{\text{spec}} = 1.20$ and a $z_{\text{phot}} = 1.85$. It appears that the relatively large Δz for this object is due to an error in the spectroscopic redshift where noise is being mistaken for an emission line yielding a lower-redshift solution than the photometric redshift. Visually inspecting the 1D and 2D spectra for this object (Figure 5.3) reveals that the location of the Hα and [OIII] + Hβ emission lines are more consistent with a spectroscopic redshift of $z_{\text{spec}} = 1.89$, and is much more in line with the photometric redshift. Thus, we plot this updated spectroscopic redshift in Figure 5.2, list it in Table 4, and use this value in calculating Δz for the sample. The remarkable agreement between

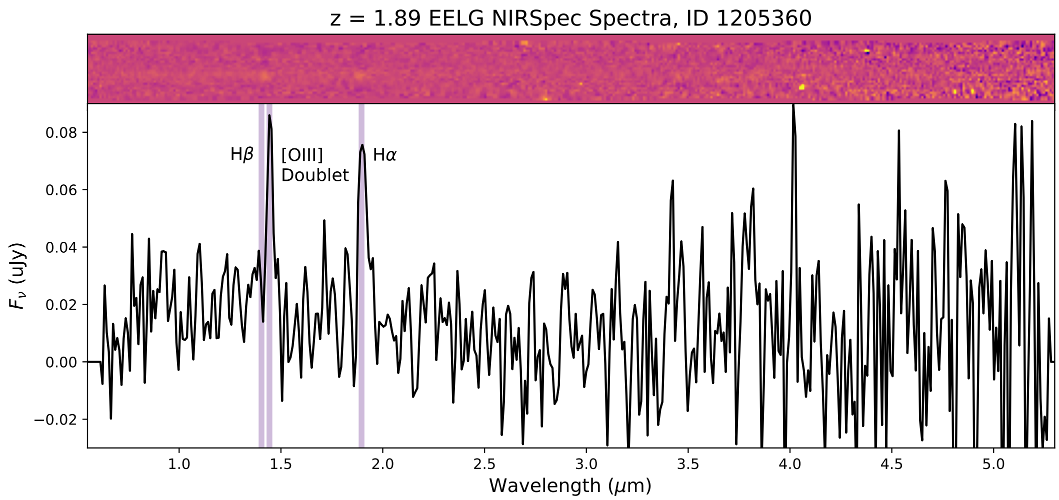

Figure 5.3: The spectrum of galaxy ID1205360 with the locations of the Hα and [OIII] + Hβ lines at a redshift of $z_{\rm spec} = 1.89$. The locations of the Hα and [OIII] + Hβ lines at that redshift lines up very well with their locations observed in the 1D spectrum. This suggests that $z_{\rm spec} = 1.89$ is the correct redshift for this object, not $z_{\rm spec} = 1.20$ as determined by the automatic pipeline.

photometric and spectroscopic redshifts confirms that not only are medium-band colour selections able to select EELGs, but they are able to do so over a *very* wide range of redshifts.

5.3 Spectroscopic Equivalent Widths

Having shown that the medium-band colour selections presented in this work are able to accurately select EELGs and determine their redshifts, the final test of these colour selections is the ability of medium-band photometry to accurately determine EWs. To verify this, the EW([OIII] + Hβ) and EW(Hα) were calculated for each of the NIRSpec spectra. The continuum fluxes need to be accurately measured in order to calculate EWs, which requires sufficient S/N in the continuum. While the Hα and [OIII] + Hβ emission lines are well detected in all 15 spectra, several galaxies had continua that were too faint to reliably calculate EWs, and were thus excluded from this analysis. Additionally, we were unable to measure the EW([OIII] + Hβ) for two galaxies, since that portion of the spectrum fell in the NIRSpec detector gaps. In total, EW(Hα) was calculated for ten spectra,

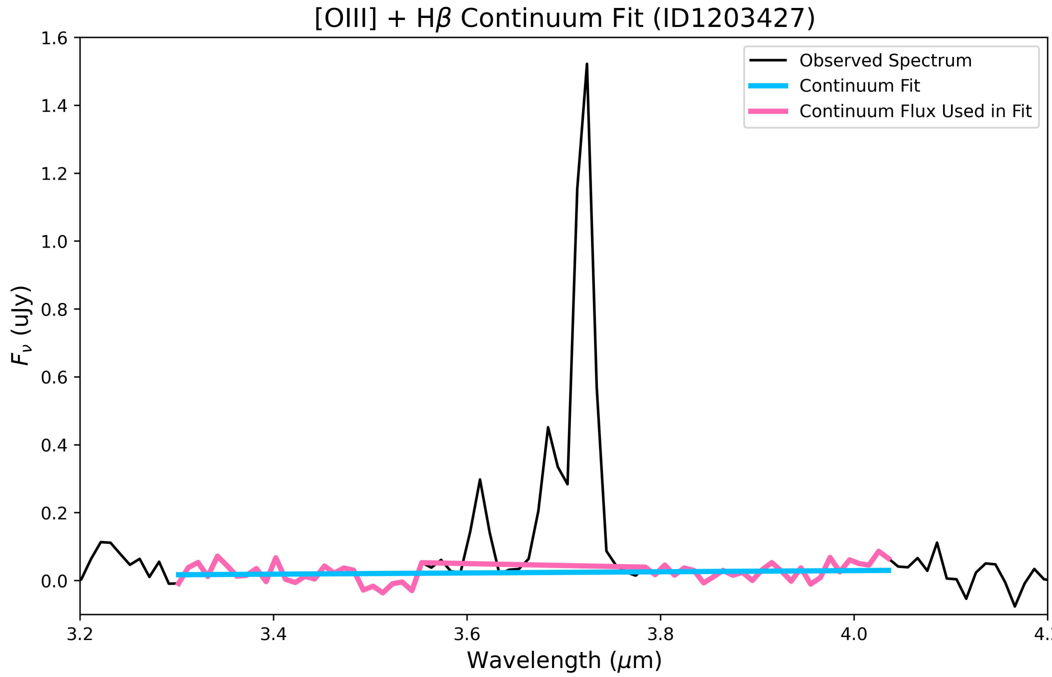

Figure 5.4: Example of the continuum fitting performed to calculate EWs from the spectra. This example shows the continuum fit for the [OIII] + Hβ lines of galaxy ID1203427.

and EW([OIII] + Hβ) was calculated for thirteen. The EW measurements are summarized in Col. 5 and Col. 7 of Table 4, which includes indicating which spectra do not include measurements of which emission lines.

For this set of galaxies, the EW([OIII] + Hβ) and EW(Hα) were measured by fitting the continuum surrounding the emission lines with a straight line, which was then used to estimate the underlying continuum emission. An example of this process is shown in Figure 5.4, which shows the continuum fit to the [OIII] + Hβ lines for ID1203427 (the first example in Figures 4.2 and 5.1). Due to the small number of spectra, the continuum fits for each line were visually inspected to ensure they provide accurate continuum estimates.

5.3.1 Accuracy of EWs Measured Through Medium-Band Photometry

Figure 5.5 plots the EW(Hα) (top) and EW([OIII] + Hβ) (bottom) calculated from photometry versus spectroscopy. The spectra confirm that it is possible to accurately calculate EWs from medium-band photometry, including confirmation that very high EW systems, with EW > 1000Å up to EW ~ 3000Å do exist. This is particularly true for EW(Hα), shown in the top panel. The EW(Hα) calculated from photometry vs. spectroscopy are in very good agreement, with a mean absolute deviation of ΔEW(Hα) $= 199$Å, RMS scatter of 320Å, and $\langle EW_{phot} - EW_{spec} \rangle = 123$Å. Interestingly, though, the same cannot be said for EW([OIII] + Hβ). While there are several EWs measured from photometry that agree with those measured through the spectroscopy (to within $\sim 100-200$Å), in general, the agreement between the two values is significantly worse for EW([OIII] + Hβ) than for EW(Hα). This time, there is a mean absolute deviation of ΔEW([OIII] + Hβ) $= 442.2$Å, RMS scatter of 538Å, and and $\langle EW_{phot} - EW_{spec} \rangle = 127$Å when measured through photometry vs. spectroscopy. The mean absolute deviation and RMS scatter are significantly larger for EW([OIII] + Hβ) than for EW(Hα), and includes cases where the difference is ΔEW([OIII] + Hβ) ~ 800Å.

5.3.2 Errors in EW Estimates from Medium-Band Photometry

There are likely two sources of error that drives the disagreement between EWs measured from photometry and spectroscopy. The first is uncertainties in measuring the continuum emission when calculating EWs using medium-band photometry. While the continuum fitting procedure described in §4.2 is able to accurately fit the continuum in many cases (such as the example in Figure 4.3) there are also cases such as that shown in Figure 5.6 where the fit is poor. The likely cause of this is the presence of other emission lines which can contaminate one or more of the filters used to estimate the continuum, which causes the continuum to be poorly constrained in those regions and results in incorrect EW measurements. While care was taken to avoid strong emission lines when estimating the continuum, certain regions of the spectrum are heavily contaminated, which makes it challenging to obtain clean continuum measurements in some cases. This is supported by the presence of other emission lines in some of the spectra, as discussed in §5.1.

This issue is of particular concern for lower-redshift galaxies and when calculating EW([OIII] + Hβ). This is because the redshifting effect makes it easier to obtain clean measurements of the

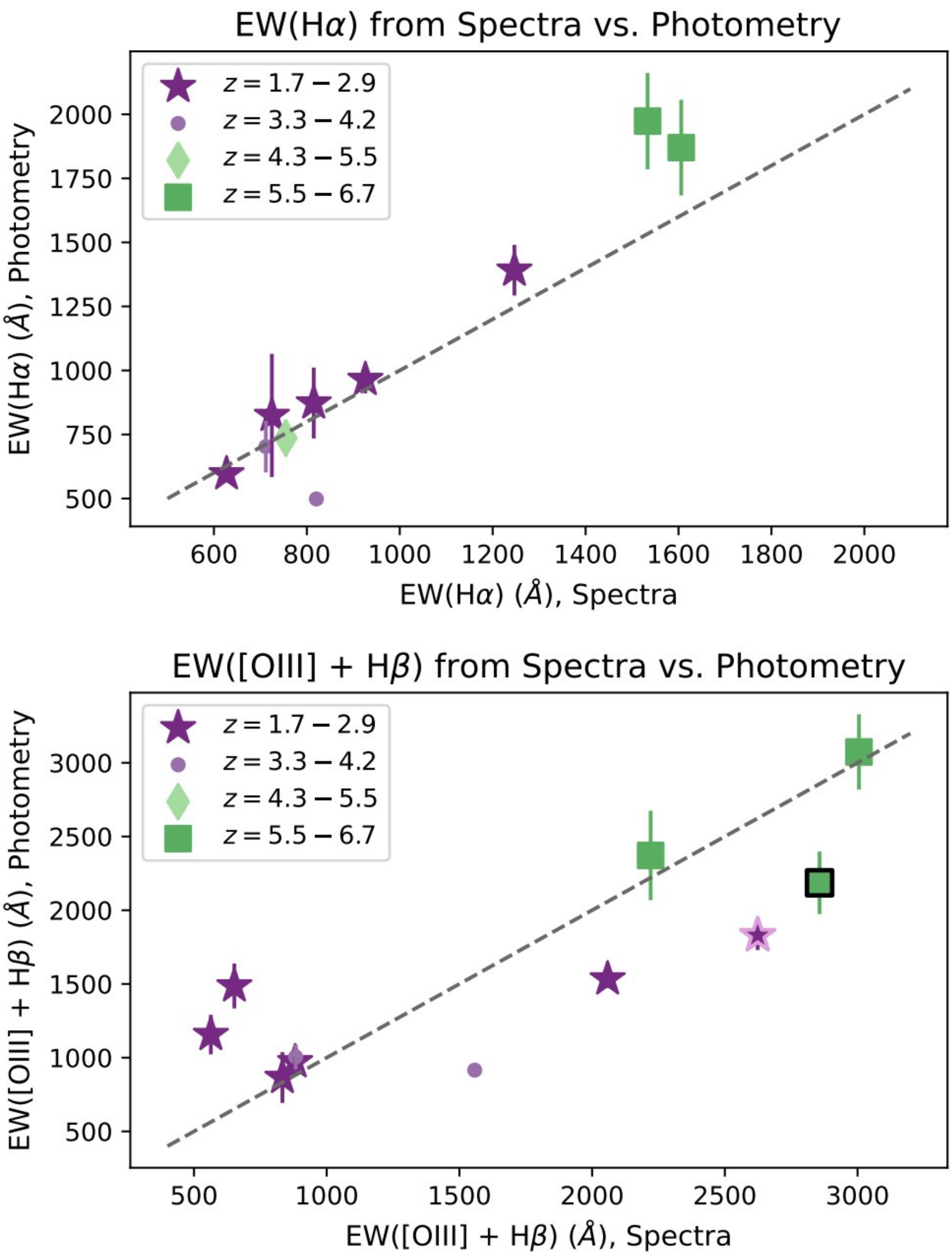

Figure 5.5: EW(Hα) (top) and EW([OIII] + Hβ) (bottom) calculated from the NIRSpec spectra vs. the medium-band photometry. In two of the spectra, the [OIII] + Hβ emission lines are "on the edge" of the filter used to estimate the EWs (as discussed in §5.3.2). These are indicated by a light outline (corrected EW calculated using a wide band instead of medium-band) and dark outline (not corrected).

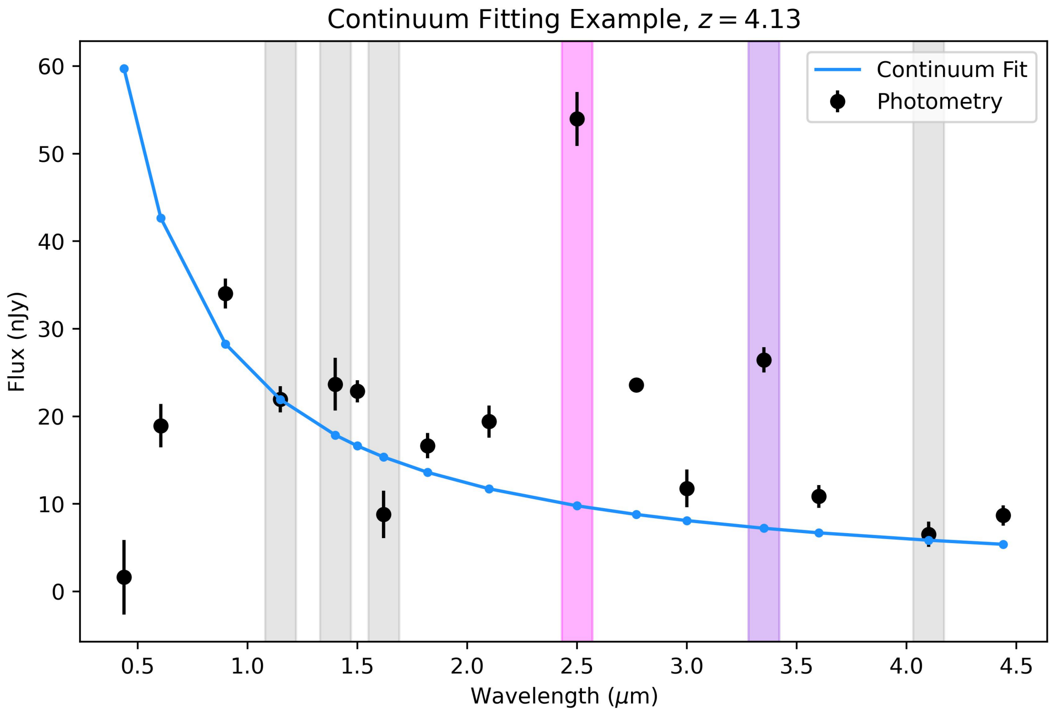

Figure 5.6: Example of continuum fitting described in §4.2. This example provides a relatively poor continuum fit, and these errors can make the final EW measurement inaccurate.

continuum for higher-redshift galaxies than for lower-redshift galaxies. In terms of measuring the EW([OIII] + Hβ), that region of the spectrum is heavily contaminated with other emission lines, much more so than the region surrounding the Hα line which is much cleaner. This is reflected in Figure 5.5, where the disagreement between spectroscopically and photometrically measured EWs is worse for [OIII] + Hβ than for Hα, and is on average worse for lower-redshift galaxies than for higher-redshift galaxies.

It may be possible to mitigate this issue by measuring the continuum using the SED fits from `EAZY` (see §4.1) instead of fitting the continuum as described in §4.2. This has the benefit of being able to measure the continuum from specific places in galaxy SEDs that are known to be completely free of contamination from other emission lines, unlike with the continuum fitting. As can be seen in Figure 4.2, the `EAZY` fits generally provide very good continuum fits when including the templates set from Larson et al. 2022, which suggests that this method will be a viable alternative to measuring the continuum.

In terms of the second source of error, the EWs were calculated assuming all of the flux from a given emission line complex falls in one filter. However, this assumption does not always hold true and can lead to EWs being underestimated when calculated from flux excesses in one filter. This phenomenon is observed in two of our spectra, shown in Figure 5.7 and reflected in Figure 5.5 as the data points with the light and black outlines. In the first case (ID1203638, plotted with the black outline in Figure 5.5) the F335M filter was used to estimate flux from the [OIII] + Hβ lines (f_{observed} in Eq. 7). The [OIII] doublet is fully contained in F335M, but the Hβ line is "on the edge" of the filter and is partially in F300M. In the second case, (ID1202026, plotted with the light outline in Figure 5.5), the F140M filter is used to estimate the flux excess from the [OIII] + Hβ complex. Since this object is at a lower redshift than the first one, the [OIII] + Hβ lines are not resolved. The exact locations of the [OIII] doublet and Hβ lines are shown in Figure 5.7, which shows that none of the Hβ flux is contained in F162M, and most of the [OIII] doublet flux is also not contained in F162M.

In the case of the second object (ID1202026), it is straightforward to recalculate the EW from the photometry, since the [OIII] + Hβ complex is fully contained in an overlapping wide band filter, F150W. When using the F162M filter to measure EW([OIII] + Hβ), we obtain a value of $\text{EW}_{F162M} = 1295$Å, which leaves a ΔEW([OIII] + Hβ)$\sim$ 1300Å difference between the value measured from the spectrum, $\text{EW}_{spec} = 2624$Å. When EW([OIII] + Hβ) is re-calculated using the overlapping wide band F150W, we obtain a value of $\text{EW}_{F150W} = 1830$Å, an improvement of $\sim$ 500Å. This is more in line with the value measured from the spectrum, and is the value plotted in Figure 5.5 (as the light outline) and used when determining the median ΔEW([OIII] + Hβ) reported in §5.3.1. Unfortunately in the first example (ID1203638), the [OIII] + Hβ complex is not found in an overlapping filter and the EW was not recalculated. Thus we report the EW estimated by using F335M to measure the flux excess, with the caveat that this value is underestimated. In this case, the difference between the EW measured from spectroscopy and photometry is of ΔEW([OIII] + Hβ) $\sim$ 700Å, which is greater than the mean absolute difference ΔEW([OIII] + Hβ) of the sample.

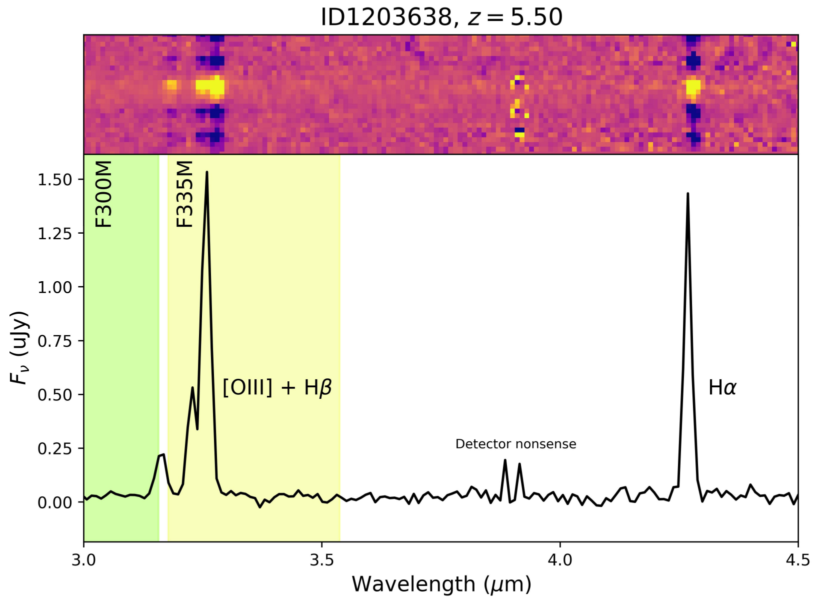

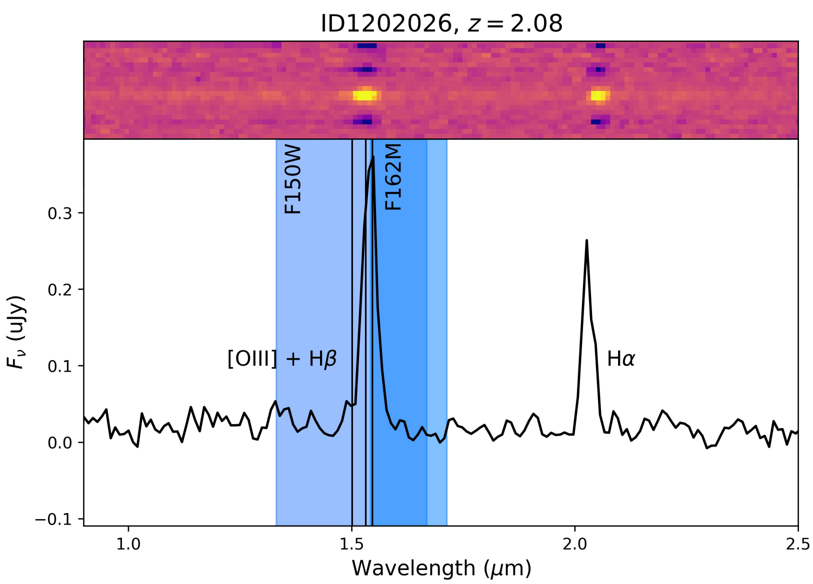

Figure 5.7: Two spectra that show the [OIII] + Hβ emission lines are partially out of the medium-band filters used to estimate the EWs. Each plot includes the filter originally used to estimate the EW (F162M for the top and F335M for the bottom) as well as overlapping (top, F150W) or neighbouring (bottom, F300M) filters. The bottom panel (ID1202026) also has the location of the Hβ, [OIII]λ4959, and [OIII]λ5007 lines labelled with the vertical black lines.

The improved measurement of EW([OIII] + Hβ) from the second object (ID1202026) is encouraging, and suggests that this "missing flux" issue is solvable. However, there is still a nearly ΔEW([OIII] + Hβ) $\sim$ 800Å difference between the EWs measured from photometry and spectroscopy, demonstrating that more work is required to fully fix this issue. In the case of the second object, this will involve improving EWs measured from the photometry as discussed above. In terms of the first object (ID1203638), improving EWs measured from the photometry will be more complicated. The lack of an overlapping wide band filter means that the only way to accurately measure the EW is by using two filters to estimate the emission line flux. While this can be done, it is complicated as it requires accounting for the filter throughput curves of the two filters that have emission line flux, as well as accounting for any part of the emission lines that do not fall in any of the filters. Unlike with continuum measurements, it appears that `EAZY` fits cannot be always used to measure emission line flux. The third example in Figure 4.2 (ID1205006) shows good agreement between the observed and predicted photometry in bands with [OIII] + Hβ and Hα flux excesses. However, the first two examples (ID1203427 and 1202967) have fairly large differences between the observed and predicted fluxes in bands with [OIII] + Hβ emission. This means that the `EAZY` SED fits cannot be reliably used to measure emission line flux, at least not with the current templates used in the SED fitting.

An additional challenge of fixing this issue lies with identifying which galaxies are affected by this in the first place. When using photometric redshifts to identify galaxies with emission line flux missing from the filter used to measure the line fluxes, we identify eight objects that suffer from this issue (one missing flux from Hα and seven missing flux from [OIII] + Hβ). However, when using the available spectroscopic redshifts to search for objects with this "missing flux", only two such objects are found (the one shown in Figure 5.7). This is a significantly higher fraction than what is found when using the photometric redshifts ($\sim$ 15% of the objects with spectroscopic redshifts vs. $\sim$ 7% of objects with photometric redshifts), and might suggest that the photometric redshifts alone are not enough to determine if an emission line is missing flux in a filter. Once again, this is a complex but fixable issue, which can likely be solved by analysing the flux excesses in neighbouring/overlapping filters and incorporating information on the photometric redshifts.

Overall, discrepancies in EWs measured from spectroscopy and photometry demonstrates that a more detailed method is required to accurately calculate EWs from medium-band photometry. However, given the very *simple* methods used to measure EWs in this work, our present analysis reveals a remarkable agreement between EWs measured using photometry and spectroscopy. A more detailed calculation of EWs from medium-band photometry appears to be a quite complex issue, however, the results in this section suggest that this issue is solvable.

5.4 Summary

NIRSpec spectroscopy of 15 of the galaxies in our sample are used to assess the ability of the medium-band colour selections/photometry to select EELGs and determine their redshifts and EWs. Figure 5.1 shows three of the spectra (corresponding to the examples in Figure 4.2), and in all cases the spectra confirm the nature of the EELGs. This includes the very red object (ID1205006) for which the Lyman break cannot be observed. Additionally, the spectroscopic redshifts of all 15 spectra are in remarkably good agreement with the photometric redshifts (Figure 5.2), verifying that the colour selections can accurately determine the redshifts of selected EELGs.

The situation is more complicated when assessing the ability of the medium-bands to accurately measure EWs. Figure 5.5 shows very good agreement between EW(Hα) measured from photometry and spectroscopy, but the agreement is much worse for EW([OIII] + Hβ). This disagreement is likely caused by two things. First is errors in accurately estimating the continuum emission when measuring EWs from medium-band photometry, which propagates into errors in the EW measurements. The likely cause of these errors is contamination from other emission lines in bands used to estimate the continuum. While care was taken to ensure those filters did not include strong emission lines, certain areas of the spectrum are heavily contaminated which makes accurate continuum measurements challenging. The second issue is caused by the assumption that 100% of the emission line flux is contained in a single filter which is then used to estimate the emission line flux. This assumption does not always hold true and can lead to EWs being underestimated when measured using medium-band photometry.

Both of these issues appear to be fixable, but will require more complex algorithms and more detailed treatments of EW measurements from medium-band photometry. While there is still some work to be done to improve EW measurements from medium-band photometry, it is worth emphasising that the results presented here are encouraging. In many cases, EWs can be accurately measured from their medium-band photometry using very *simple* methods, which suggests that incorporating more complex techniques will be able to substantially improve the accuracy of EW measurements.

6 Summary and Future Work

This thesis presents a sample of EELGs selected using NIRCam medium-band colour selections. The data set used in this work (§2) is provided by CANUCS, which includes deep medium-band photometry making it ideal for this work. The colour selections (§3) were defined using a set of SPS models of EELGs as well as models of other galaxy populations which could contaminate the EELG sample. Based on these models, we define a set of ten colour selections (Table 3) which are able to select EELGs with both extreme Hα and [OIII] + Hβ emission over $1.6 \lesssim z \lesssim 6.7$. These sources include typical EELGs, but also include some very red galaxies (see the third example (ID 1205006) in Figure 4.2, 5.1), which have continuum fluxes rewards of the Lyman break that are so faint that a Lyman break cannot be observed. Objects such as these demonstrate the ability of our colour cuts to select galaxies on emission line flux, with no dependence on continuum emission. Thus, we show medium-band colour selections are a powerful tool that can identify very faint galaxies which may play an important role in reionization, and objects that contaminate photometrically selected samples of very high-redshift galaxies (such as ID 1205006).

We calculate the EWs (§4.2) and physical properties (§4.3) of the EELGs in our sample. They all have very high [OIII] + Hβ and Hα EWs, sometimes up to ~ 3000Å, and their properties are typical of EELGs: low mass, low metallicity, high SSFRs, and generally compact morphologies.

Additionally, we show that the EELGs in our sample follow trends of increasing EW(Hα) and EW([OIII] + Hβ) with redshift, an anti-correlation between EW(Hα) and stellar mass, no correlation between EW([OIII] + Hβ) and stellar mass, increasing SSFR with redshift, and follow the "star-forming main sequence" (§4.2, 4.3, Figures 4.6, 4.7). Finally, we present follow-up NIRSpec spectroscopy of 15 of these sources (§5). These spectra confirm that medium-band colour cuts are able to efficiently select EELGs over a wide range of redshifts (§5.1, 5.2), and can be used to measure EWs remarkably well given the simple methods used in this work (§5.3). That said, we do note the need for a more detailed method of calculating EWs from the photometry as significant discrepancies between EWs measured from photometry and spectroscopy do exist for EW([OIII] + Hβ). Improving the EW measurements is a goal of future work. These improvements will involve more complex filter convolution algorithms when calculating EWs from photometry, developing an algorithm capable of identifying and measuring EWs when emission lines are not fully contained in a single filter, and improving continuum measurements (e.g. using SED fits to measure the continuum). In conclusion, this work shows that medium-band photometry is effective at identifying EELGs over a very wide range of redshifts, and can generally be used to measure their EWs.

It is important to reiterate that the colour selections used in this work target the brightest and most extreme EELGs with both strong Hα and [OIII] + Hβ emission, in only the first of five CANUCS flanking fields. This leaves open many avenues for future work that will allow us to significantly expand the sample of galaxies presented here. These include searches for fainter and less extreme EELGs, colour selections involving only one emission line complex, incorporation of full photometric redshift fitting with appropriate templates, and analysis of the remaining four CANUCS NIRCam flanking fields. Additionally, we plan to incorporate observations from the program "*JWST in Technicolour: Finding and Mapping the Most Extreme Star Forming Galaxies in the Epoch of Reionization with Medium and Narrow Bands*" (GO ID 3362) into future work. This program will provide follow-up observations on three of the CANUCS fields in three broad (F070W, F200W, F356W), two narrow (F164N, F187N), and three medium (F430M, F460M, F480M) band filters. The red medium-bands will be of particular importance to future work, as they will enable searches for the highest-redshift EELGs including [OIII] + Hβ emitters at $z \sim 7-9$ and [OII] emitters at $z \sim 10-12$. Searching for these objects is challenging with the existing CANUCS data set, since the wavelength range covered by the new medium-bands ($\lambda \sim 4.3-5\mu$m) is only observed by a single broad-band filter (F444W) in CANUCS. When combined with CANUCS, the new bands in *JWST in Technicolour* will allow for the selection of very ultra-faint, emission line only sources which have been shown to exist in the EoR (e.g. Atek et al. 2023 as discussed in §1.4).

Bibliography

Adams N. J., Bowler R. A. A., Jarvis M. J., Varadaraj R. G., Häußler B., 2023, Monthly Notices of the Royal Astronomical Society, 523, 327

Arrabal Haro P., et al., 2023, Technical report, Spectroscopic verification of very luminous galaxy candidates in the early universe, https://ui.adsabs.harvard.edu/abs/2023arXiv230315431A, doi:10.48550/arXiv.2303.15431. , https://ui.adsabs.harvard.edu/abs/2023arXiv230315431A

Asada Y., et al., 2022, Technical report, JWST catches the assembly of a \z\textbackslashsim5\ ultra-low-mass galaxy, https://ui.adsabs.harvard.edu/abs/2022arXiv221207540A, doi:10.48550/arXiv.2212.07540. , https://ui.adsabs.harvard.edu/abs/2022arXiv221207540A

Atek H., et al., 2023, First spectroscopic observations of the galaxies that reionized the Universe, doi:10.48550/arXiv.2308.08540, https://ui.adsabs.harvard.edu/abs/2023arXiv230808540A

Boyett K., et al., 2022, The Astrophysical Journal, 940, L52

Brammer G. B., van Dokkum P. G., Coppi P., 2008, The Astrophysical Journal, 686, 1503

Böker T., et al., 2023, Publications of the Astronomical Society of the Pacific, 135, 038001

Calzetti D., 2001, Publications of the Astronomical Society of the Pacific, 113, 1449

Cardamone C., et al., 2009, Monthly Notices of the Royal Astronomical Society, 399, 1191

Conroy C., Gunn J. E., 2010, The Astrophysical Journal, 712, 833

Conroy C., Gunn J. E., White M., 2009, The Astrophysical Journal, 699, 486

Endsley R., Stark D. P., Chevallard J., Charlot S., 2021, Monthly Notices of the Royal Astronomical Society, 500, 5229

Endsley R., Stark D. P., Whitler L., Topping M. W., Chen Z., Plat A., Chisholm J., Charlot S., 2022, Technical report, A JWST/NIRCam Study of Key Contributors to Reionization: The

Star-forming and Ionizing Properties of UV-faint z sim 7-8 Galaxies, https://ui.adsabs.harvard.edu/abs/2022arXiv220814999E, doi:10.48550/arXiv.2208.14999. , https://ui.adsabs.harvard.edu/abs/2022arXiv220814999E

Endsley R., et al., 2023a, The Star-forming and Ionizing Properties of Dwarf z~6-9 Galaxies in JADES: Insights on Bursty Star Formation and Ionized Bubble Growth, doi:10.48550/arXiv.2306.05295, https://ui.adsabs.harvard.edu/abs/2023arXiv230605295E

Endsley R., Stark D. P., Whitler L., Topping M. W., Chen Z., Plat A., Chisholm J., Charlot S., 2023b, Monthly Notices of the Royal Astronomical Society, 524, 2312

Finlator K., Muñoz J. A., Oppenheimer B. D., Oh S. P., Özel F., Davé R., 2013, Monthly Notices of the Royal Astronomical Society, 436, 1818

Fujimoto S., et al., 2023, UNCOVER: A NIRSpec Census of Lensed Galaxies at z=8.50-13.08 Probing a High AGN Fraction and Ionized Bubbles in the Shadow, doi:10.48550/arXiv.2308.11609, https://ui.adsabs.harvard.edu/abs/2023arXiv230811609F

Gnedin N. Y., 2014, The Astrophysical Journal, 793, 29

Gupta A., et al., 2023, Monthly Notices of the Royal Astronomical Society, 519, 980

Henry A., Berg D. A., Scarlata C., Verhamme A., Erb D., 2018, The Astrophysical Journal, 855, 96

Iyer K. G., Gawiser E., Faber S. M., Ferguson H. C., Kartaltepe J., Koekemoer A. M., Pacifici C., Somerville R. S., 2019, The Astrophysical Journal, 879, 116

Izotov Y. I., Guseva N. G., Fricke K. J., Henkel C., Schaerer D., Thuan T. X., 2021, Astronomy and Astrophysics, 646, A138

Kashino D., Lilly S. J., Matthee J., Eilers A.-C., Mackenzie R., Bordoloi R., Simcoe R. A., 2022, Technical report, EIGER I. a large sample of [OIII]-emitting galaxies at $5.3 < z < 6.9$ and direct evidence for local reionization by galaxies, https://ui.adsabs.harvard.edu/abs/2022arXiv221108254K, doi:10.48550/arXiv.2211.08254. , https://ui.adsabs.harvard.edu/abs/2022arXiv221108254K

Kewley L. J., Nicholls D. C., Sutherland R. S., 2019, Annual Review of Astronomy and Astrophysics, 57, 511

Kron R. G., 1980, The Astrophysical Journal Supplement Series, 43, 305

Kroupa P., 2001, Monthly Notices of the Royal Astronomical Society, 322, 231

Laporte N., Ellis R. S., Witten C. E. C., Roberts-Borsani G., 2022, Technical report, Resolving Ambiguities in the Inferred Star Formation Histories of Intense [O III] Emitters in the Reionisation Era, https://ui.adsabs.harvard.edu/abs/2022arXiv221205072L, doi:10.48550/arXiv.2212.05072. , https://ui.adsabs.harvard.edu/abs/2022arXiv221205072L

Larson R. L., et al., 2022, Technical report, Spectral Templates Optimal for Selecting Galaxies at z $\sim$ 8 with JWST, https://ui.adsabs.harvard.edu/abs/2022arXiv221110035L, doi:10.48550/arXiv.2211.10035. , https://ui.adsabs.harvard.edu/abs/2022arXiv221110035L

Liu S., et al., 2022, The Astrophysical Journal, 927, 57

Mascia S., et al., 2023, Astronomy and Astrophysics, 672, A155

Maseda M. V., et al., 2014, The Astrophysical Journal, 791, 17

Maseda M. V., et al., 2018, The Astrophysical Journal, 854, 29

Matthee J., Mackenzie R., Simcoe R. A., Kashino D., Lilly S. J., Bordoloi R., Eilers A.-C., 2022, Technical report, EIGER II. first spectroscopic characterisation of the young stars and ionised gas associated with strong Hβ and [OIII] line-emission in galaxies at z=5-7 with JWST, https://ui.adsabs.harvard.edu/abs/2022arXiv221108255M, doi:10.48550/arXiv.2211.08255. , https://ui.adsabs.harvard.edu/abs/2022arXiv221108255M

McGreer I. D., Mesinger A., D'Odorico V., 2015, Monthly Notices of the Royal Astronomical Society, 447, 499

McKinney J., et al., 2023, The Astrophysical Journal, 946, L39

Mingozzi M., et al., 2022, The Astrophysical Journal, 939, 110

Nanayakkara T., et al., 2020, The Astrophysical Journal, 889, 180

Onodera M., et al., 2020, The Astrophysical Journal, 904, 180

Paardekooper J.-P., Khochfar S., Dalla Vecchia C., 2015, Monthly Notices of the Royal Astronomical Society, 451, 2544

Pei Y. C., 1992, The Astrophysical Journal, 395, 130

Popesso P., et al., 2022, Monthly Notices of the Royal Astronomical Society, 519, 1526

Reddy N. A., et al., 2018, The Astrophysical Journal, 869, 92

Reddy N. A., et al., 2022, The Astrophysical Journal, 926, 31

Rhoads J. E., et al., 2023, The Astrophysical Journal, 942, L14

Rieke M. J., et al., 2023, Publications of the Astronomical Society of the Pacific, 135, 028001

Rigby J., et al., 2023, Publications of the Astronomical Society of the Pacific, 135, 048001

Rinaldi P., et al., 2023, Technical report, Strong (Hb + [OIII]) and Ha emitters at redshift z \textbackslashtextasciitilde 7-8 unveiled with JWST/NIRCam and MIRI imaging in the Hubble eXtreme Deep Field (XDF), https://ui.adsabs.harvard.edu/abs/2023arXiv230110717R, doi:10.48550/arXiv.2301.10717. , https://ui.adsabs.harvard.edu/abs/2023arXiv230110717R

Roberts-Borsani G. W., et al., 2016, The Astrophysical Journal, 823, 143

Roberts-Borsani G., Treu T., Mason C., Schmidt K. B., Jones T., Fontana A., 2021, The Astrophysical Journal, 910, 86

Robertson B. E., 2022, Annual Review of Astronomy and Astrophysics, 60, 121

Robertson B. E., Ellis R. S., Furlanetto S. R., Dunlop J. S., 2015, The Astrophysical Journal, 802, L19

Saxena A., et al., 2023, JADES: The production and escape of ionizing photons from faint Lyman-alpha emitters in the epoch of reionization, doi:10.48550/arXiv.2306.04536, https://ui.adsabs.harvard.edu/abs/2023arXiv230604536S

Schaerer D., Marques-Chaves R., Barrufet L., Oesch P., Izotov Y. I., Naidu R., Guseva N. G., Brammer G., 2022, Astronomy and Astrophysics, 665, L4

Shapley A. E., Sanders R. L., Reddy N. A., Topping M. W., Brammer G. B., 2023, The Astrophysical Journal, 954, 157

Shimizu I., Inoue A. K., Okamoto T., Yoshida N., 2014, Monthly Notices of the Royal Astronomical Society, 440, 731

Smit R., et al., 2014, The Astrophysical Journal, 784, 58

Smit R., et al., 2015, The Astrophysical Journal, 801, 122

Speagle J. S., Steinhardt C. L., Capak P. L., Silverman J. D., 2014, The Astrophysical Journal Supplement Series, 214, 15

Stark D. P., Schenker M. A., Ellis R., Robertson B., McLure R., Dunlop J., 2013, The Astrophysical Journal, 763, 129

Stark D. P., et al., 2017, Monthly Notices of the Royal Astronomical Society, 464, 469

Stefanon M., Bouwens R. J., Illingworth G. D., Labbé I., Oesch P. A., Gonzalez V., 2022, The Astrophysical Journal, 935, 94

Sun F., et al., 2022, Technical report, First Sample of Halpha+[OIII] 5007 Line Emitters at z > 6 through JWST/NIRCam Slitless Spectroscopy: Physical Properties and Line Luminosity Functions, https://ui.adsabs.harvard.edu/abs/2022arXiv220903374S, doi:10.48550/arXiv.2209.03374. , https://ui.adsabs.harvard.edu/abs/2022arXiv220903374S

Tang M., Stark D. P., Chevallard J., Charlot S., 2019, Monthly Notices of the Royal Astronomical Society, 489, 2572

Tang M., Stark D. P., Ellis R. S., 2022, Monthly Notices of the Royal Astronomical Society, 513, 5211

Taylor A. J., Barger A. J., Cowie L. L., 2022, The Astrophysical Journal, 939, L3

Terao Y., Spitler L. R., Motohara K., Chen N., 2022, The Astrophysical Journal, 941, 70

Tran K.-V. H., et al., 2020, The Astrophysical Journal, 898, 45

Trump J. R., et al., 2022, Technical report, The Physical Conditions of Emission-Line Galaxies at Cosmic Dawn from JWST/NIRSpec Spectroscopy in the SMACS 0723 Early Release Observations, https://ui.adsabs.harvard.edu/abs/2022arXiv220712388T, doi:10.48550/arXiv.2207.12388. , https://ui.adsabs.harvard.edu/abs/2022arXiv220712388T

Williams C. C., et al., 2023, Technical report, JEMS: A deep medium-band imaging survey in the Hubble Ultra-Deep Field with JWST NIRCam & NIRISS, https://ui.adsabs.harvard.edu/abs/2023arXiv230109780W, doi:10.48550/arXiv.2301.09780. , https://ui.adsabs.harvard.edu/abs/2023arXiv230109780W

Willott C. J., et al., 2022, Publications of the Astronomical Society of the Pacific, 134, 025002

Withers S., et al., 2023, Spectroscopy from Photometry: A Population of Extreme Emission Line Galaxies at \$1.7 \lesssim z \lesssim 6.7\$ Selected with JWST Medium Band Filters, doi:10.48550/arXiv.2304.11181, https://ui.adsabs.harvard.edu/abs/2023arXiv230411181W

Zackrisson E., Rydberg C.-E., Schaerer D., Östlin G., Tuli M., 2011, The Astrophysical Journal, 740, 13

Zackrisson E., et al., 2017, The Astrophysical Journal, 836, 78

Zavala J. A., et al., 2023, The Astrophysical Journal, 943, L9 van der Wel A., et al., 2011, The Astrophysical Journal, 742, 111